



**Microstructural evolution and reverse flow in shear-banding  
of entangled polymer melts**

Journal:	<i>Soft Matter</i>
Manuscript ID	SM-ART-10-2022-001337.R2
Article Type:	Paper
Date Submitted by the Author:	02-Dec-2022
Complete List of Authors:	Boudaghi-Khajehnohar, Mahdi; University of Tennessee Knoxville College of Engineering, Chemical and Biomolecular Engineering Edwards, Brian; University of Tennessee Knoxville College of Engineering, Chemical and Biomolecular Engineering Khomami, Bamin; University of Tennessee, Chemical and Biomolecular Engineering

Cite this: DOI: 00.0000/xxxxxxxxxx

## Microstructural evolution and reverse flow in shear-banding of entangled polymer melts<sup>†</sup>

Mahdi Boudaghi,<sup>a</sup> Brian J. Edwards,<sup>\*a</sup> and Bamin Khomami<sup>\*a</sup>

Received Date

Accepted Date

DOI: 00.0000/xxxxxxxxxx

The temporal and spatial evolution of shear banding under startup of shear flow was simulated for highly entangled, linear, monodisperse polyethylene melts of differing molecular length,  $C_{750}H_{1502}$ ,  $C_{1200}H_{2402}$ , and  $C_{3000}H_{6002}$ , using a high-fidelity coarse-grained dissipative particle dynamics method. It was determined that shear stress was dominated by segmental orientation of entangled strands at low shear rates, but at a critical shear rate below the reciprocal of the Rouse time, flow-induced disentanglement resulted in the onset of chain tumbling that reduced the average degree of orientation, leading to a regime of decreasing shear stress, with a commensurate onset of increasing average chain extension imposed by the strong flow kinematics that ultimately drove the steady-state shear stress higher. During startup of shear flow, shear band development began immediately after the maximum in the first normal stress difference, where distinct fast and slow bands formed. The slow bands consisted of relatively entangled and coiled molecules, whereas the fast bands consisted of more disentangled and extended chains that experienced quasiperiodic rotation/retraction cycles. The simulation results often exhibited a generation of temporary reverse flow, in which the local fluid velocity was temporarily opposite to that of the bulk flow direction, at the onset of the shear-banding phenomena; this effect was consistent with earlier experiments and theoretical results. The physical mechanism for the generation of reverse flow during shear-band formation was investigated and found to be related to the recoil of the molecules comprising the slow band. Overall, the phenomenon of shear banding appeared to arise due to flow-induced disentanglement from orientational ordering and segmental stretching that affected individual chains to different degrees, ultimately resulting in regions of relatively coiled and entangled chains that evolved into a slow band, whereas the locally disentangled chains, experiencing quasiperiodic stretch-rotation cycles, formed a fast band. The transitional period resulted in a kinematic instability that generated the temporary reverse-flow phenomenon.

### 1 Introduction

The physical properties of industrial products formed from molten polymers are typically strongly dependent on the processing flow kinematics, which is primarily a result of the process kinematic and thermal history on the inherent microstructure of the entangled polymers. Flow-induced instabilities, such as shear banding and surface fracture, which affect the process kinematics, can result in highly unpredictable and undesirable physical properties of the formed products, such as sharkskin, melt fracture, and extrudate distortion. These instabilities often arise due to the dynamics of the complex nonlinear viscoelastic response of the entangled network to the processing kinematics. These process flows provoke a wide range of dynamic responses across

a spectrum of time and length scales. Particularly, since the induced dynamics play an important role in the development of flow instabilities, it is important to understand the fundamentals of microstructure development under flow and its impact on kinematics to design and predict optimal processing methods.

Shear banding is a nonlinear response of viscoelastic materials that manifests as the spatial variation in viscosity and the localization of strain rate along the flow gradient direction<sup>1–4</sup>. It has been extensively investigated both theoretically and experimentally, as a variety of materials exhibit this behavior, including entangled polymer solutions and melts<sup>5–8</sup>, wormlike micelles<sup>9–11</sup>, liquid crystals<sup>12–14</sup>, glassy materials<sup>15–17</sup>, and biphasic liquids<sup>18</sup>.

Reptation theory predicts a steady-state shear-banding instability and associates it with the nonmonotonic constitutive shear stress versus strain rate flow curve<sup>19,20</sup>. Many analyses of step-strain startup and steady shear flows predict the separation of the flow into layers with low and high shear rates in the shear rate range of  $\dot{\gamma} > 1/\tau_d$ , where  $\tau_d$  is disengagement time, as the

<sup>a</sup> Material Research and Innovation Laboratory, Department of Chemical and Biomolecular Engineering, University of Tennessee-Knoxville, Tennessee, USA, 37996; E-mail: bje@utk.edu, bkhomami@utk.edu

steady-state shear stress decreases from its maximum value<sup>21,22</sup>. Linear stability analyses of advanced tube-based models, *e.g.* the Rolie-Poly model<sup>23</sup> that includes multiple dynamic mechanisms such as contour length fluctuation and convective constraint release, predict the development of a banded flow structure under steady-state and transient conditions<sup>24,25</sup>. Olmsted, Fielding, and coworkers studied the effect of various tuning parameters, particularly those related to the convective constraint release mechanism, on the prediction of the spatial inhomogeneity. Specifically, Moorcraft and Fielding developed a universal criterion for the onset of a banded structure based on a transient rheological response function<sup>26–28</sup>. Moreover, it has been shown that entangled polymeric solutions with a monotonic flow curve could also attain a steady-state and transient banded flow structure induced by coupling between polymer stress and concentration<sup>29</sup>. Nevertheless, despite theoretical predictions, most experimental measurements of entangled polymeric liquids revealed a monotonically increasing stress flow curve with no indication of gradient banding.

Wang and colleagues used a particle-tracking velocimetry method to observe the development of steady and transient shear banding in unidirectional shear flow experiments of entangled polymer solutions, including DNA and polybutadiene.<sup>5,6,30–34</sup> They attributed the onset of shear banding to a flow-induced cohesive failure resulting from elastic yielding of the entanglement network. Burroughs *et al.*<sup>7</sup> measured *in situ* concentration profiles in entangled 1,4-polybutadiene solutions and demonstrated shear banding arising from coupled flow and concentration gradients above a critical strain rate. Furthermore, Shin *et al.*<sup>8</sup> concluded that flow-induced disentanglement in sheared solutions of highly entangled DNA solutions was correlated with observation of shear banding in these liquids.

Despite these and other informative experiments, typical experimental measurement techniques<sup>35</sup> and continuum-level models with various tuning parameters are not descriptive enough to elucidate the detailed dynamic mechanisms that are responsible for this phenomenon. To develop a fundamental physical understanding of the manifestations of shear-banded structures, it is necessary to overcome the limitations of experiments and bulk-averaged continuum-level models; hence a detailed microscopic-level study of polymer dynamics involving atomistic or coarse-grained polymer molecules under steady-state and transient shear conditions is extremely useful for determining the true mechanistic nature of these flow instabilities.

Cao and Likhtman<sup>36</sup> performed a coarse-grained molecular dynamics study of entangled melt systems consisting of linear chains of up to 10 entanglements per chain under a step-strain startup shear flow. They observed onset of transient and steady shear banding immediately following the stress overshoot for both monotonic and nonmonotonic flow curves. Later, Mohageghi and Khomami investigated the underlying molecular mechanisms of shear banding using high-fidelity dissipative particle dynamics (DPD) simulations in moderately entangled monodisperse melts with up to 13 average entanglements per chain in step-strain and finite-strain startup shear flows. They demonstrated that shear banding occurs as a result of inhomogeneous chain segmental ori-

entation and entanglement density within the fluid for  $\dot{\gamma}$  beyond  $\sim \tau_d^{-1}$ , resulting in a change in flow stability and the formation of banded structures<sup>37–40</sup>. Moreover, they demonstrated that shear banding is not a unique response of entangled polymeric fluids to a specific shear rate<sup>38,39</sup>. To that end, when the shear rate ramp time is increased to approximately that of the chain tumbling time scale, *i.e.*,  $\tau_{rot}$ , the ratio between orientation and stretch relaxation times approaches unity; hence, stress overshoot is damped and shear banding is obviated.

Boudaghi *et al.*<sup>41</sup> studied the effect of different melt characteristics on the flow curve and the variation in the observation of transient and steady banded flow structures due to polydispersity. These authors demonstrated that the presence of a broad spectrum of relaxation times and a wide variation in single chain dynamics (namely, segmental alignment, stretching, and tumbling) in polydisperse melts resulted in a broad plateau in the steady-state shear stress response rather than a nonmonotonic profile. Furthermore, the shape and lifetime of the bands changed dramatically with the degree of polydispersity, and a criterion was established for the onset of transient shear banding based on the local Rouse time within a band as  $\dot{\gamma} \gtrsim \tau_{R_{local}}^{-1}$ .

Despite significant advances in understanding the mechanisms underlying the formation of the inhomogeneity and the transient formation of the banded structures, increasing the chain length introduces new complications that might result in additional complex phenomena. Wang and colleagues, for example, observed the emergence of reverse flow (RF), *i.e.*, stagnation and a negative velocity gradient, that emerged when the velocity profile was transforming into regions with different strain rates upon startup of shear. Similar behaviour was predicted by theoretical analysis using the Rolie-Poly model<sup>24</sup>. According to these findings, the negative velocity gradient appears shortly after the shear stress overshoot, when the eigenvalue of the stability matrix attains its maximum positive value. At later times, this value decays to a slightly negative number as the system approaches steady state. Adams and Corbert also illustrated a similar prediction of a recoiled velocity profile, *i.e.*, reverse flow, in liquid crystalline polymers using a nematic dumbbell model<sup>12</sup>.

Although a negative velocity gradient has been observed experimentally and predicted by continuum-level stability analysis, the molecular-level mechanism associated with this phenomenon has not been thoroughly investigated. To that end, it is reasonable to conjecture that this phenomenon is molecular-length dependent and is associated with a dramatic change in polymer conformation at the onset of the inhomogeneity. Evidently, high-resolution tracking of individual macromolecule conformational changes is critical to gaining a mechanistic understanding of this phenomenon. Despite advances, single-chain microscopy must be refined in order to overcome optical tracking challenges and simultaneously track multiple macromolecules on relevant time scales for use in dense polymeric fluids<sup>42–44</sup>. Recent experiments by Shin *et al.*<sup>45</sup> on entangled polymeric solutions via fluorescent DNA-bridged dumbbell probes have overcome some of the experimental issues. These experiments have revealed key details of the physical mechanisms leading to the emergence of shear bands, such as an inhomogeneous flow-induced disentanglement of the

network leading to higher orientation within the fast band, which have largely confirmed the basic molecular mechanism of shear banding in entangled polymeric melts put forth by Mohagheghi and Khomami<sup>38,39</sup>.

High-fidelity atomistic and coarse-grained mesoscopic simulations of entangled polymeric liquids offer a complementary role in elucidating the coupling between single molecule dynamics, network topology, bulk rheological properties, and flow kinematics<sup>46–52</sup>. However, attempts to improve the understanding of polymer dynamics by performing atomistic molecular dynamics simulations that use cutting-edge computational resources and numerical algorithms are limited to moderately entangled macromolecules, such as linear polyethylene (PE) chains with about 13 entanglements (C<sub>1000</sub>H<sub>2002</sub>)<sup>46,47,53</sup>. To overcome this limitation, high-fidelity dissipative particle dynamics simulations were performed that afforded the opportunity of studying much longer molecular chains while retaining the rheological and topological characteristics of the atomistic PE melts.<sup>54</sup> This technique allowed investigation of the effects of molecular length and entanglement density on the transient and steady-state flow-induced microstructure. In particular, the formation of reverse flow has been examined in the three linear polyethylene melts as a model system, represented by coarse-grained molecular chains with 250 (C<sub>750</sub>H<sub>1502</sub>), 400 (C<sub>1200</sub>H<sub>2402</sub>), and 1000 (C<sub>3000</sub>H<sub>6002</sub>) DPD particles, over a wide range of step-strain startup shear flows. Note that this is especially important to investigate the transitory RF phenomenon since earlier molecular-level simulations were unable to reproduce this experimentally observed behavior, which precluded the presentation of a comprehensive picture of the incipient and early stages of shear banding in highly entangled polymeric melts.

## 2 Simulation methodology

The simulations employed the dissipative particle dynamics force-field concept pioneered by Hoogerbrugge and Koelman<sup>55,56</sup>, which was subsequently formulated in terms of a stochastic differential equation and the corresponding Fokker-Planck equation by Español and Warren<sup>57</sup>. The force field contains a pairwise linear repulsive conservative force,  $\mathbf{F}^C$ , a dissipative force,  $\mathbf{F}^D$ , which is proportional to the velocity differences between all pairs of particles,  $\mathbf{v}_i - \mathbf{v}_j$ , and a random force,  $\mathbf{F}^R$ , which is proportional to the temperature of the material. The forces are coupled through two weighting functions for the dissipative and random forces, by definition, as  $\omega^D = (\omega^R)^2 = (1 - r_{ij}/r_c)^2$ , where  $\omega^D$  and  $\omega^R$  are the weighting functions for dissipative and random forces, respectively,  $r_c$  is the DPD cutoff distance, and  $r_{ij}$  is the distance between particle centers. Furthermore, the fluctuation-dissipation theorem establishes a connection between the viscous dissipation and system temperature as  $\sigma^2 = 2\gamma^D k_B T$ , where  $\gamma^D$ ,  $\sigma$ , and  $k_B T$  are the viscous friction coefficient, the magnitude of thermal noise, and the effective system temperature, respectively.

The DPD forces are described by the equations

$$\mathbf{F}_i^{DPD} = \sum_{j \neq i} (\mathbf{F}_{ij}^C + \mathbf{F}_{ij}^D + \mathbf{F}_{ij}^R), \quad (1)$$

$$\mathbf{F}_{ij}^C = a \left(1 - \frac{r_{ij}}{r_c}\right) \hat{\mathbf{e}}_{ij}, \quad (2)$$

$$\mathbf{F}_{ij}^D = -\gamma^D \omega^D r_{ij} [(\mathbf{v}_i - \mathbf{v}_j) \cdot \hat{\mathbf{e}}_{ij}] \hat{\mathbf{e}}_{ij}, \quad (3)$$

$$\mathbf{F}_{ij}^R = \sigma \omega^R r_{ij} \zeta \hat{\mathbf{e}}_{ij}. \quad (4)$$

In these equations, the maximum repulsive force between each pair of particles is quantified by the parameter  $a$  (which was set sufficiently large to eliminate chain crossing—see discussion in Sec. 2.1 and Table 1), with the force vanishing as the magnitude of the particle pair center-to-center vector,  $\mathbf{r}_{ij}$ , approaches the cut-off distance,  $r_c$ . In Eq. (4),  $\zeta$  is a Gaussian random variable, where  $\langle \zeta(t) \rangle = 0$  and  $\langle \zeta_{ij}(t) \zeta_{mn}(t') \rangle = (\delta_{im} \delta_{jn} + \delta_{in} \delta_{jm}) \delta(t - t')$ , where evidently  $\zeta_{ij}(t) = \zeta_{ji}(t)$ . All forces act in the direction  $\hat{\mathbf{e}}_{ij} = \mathbf{r}_{ij}/r_{ij}$  up to the DPD cutoff distance.

The intramolecular interactions consist of two contributions. The first is a bond force between adjacent particles,  $\mathbf{F}_{ik}^{spr}$ , represented by a harmonic spring,  $\mathbf{U}_{ik}^{spr} = k_{spr}(r_{eq} - r_{ik})^2/2$ , for  $k = i \pm 1$ , where  $k_{spr}$  is the force constant and  $r_{ik}$  and  $r_{eq}$  are the distances between adjacent particle centers and the equilibrium bond distance, respectively. The second is a bending force,  $\mathbf{F}_{il}^{bend} = k_{bend}(1 - \sin(\theta))$ , which is derived from the potential  $\mathbf{U}_{il}^{bend} = k_{bend}(1 + \cos(\theta))$ , for  $l = i \pm 2$ , where  $k_{bend}$  and  $\theta$  are the bending potential coefficient and the angle between three neighboring particles along the chain backbone. Thus, the total force on each polymer particle  $i$ ,  $\mathbf{F}_i^{tot}$ , is represented as

$$\mathbf{F}_i^{tot} = \mathbf{F}_i^{DPD} + \sum_k^{i \pm 1} \mathbf{F}_{ik}^{spr} + \sum_l^{i \pm 2} \mathbf{F}_{il}^{bend}. \quad (5)$$

This expression for the force on each particle is inserted into Newton's second law of motion and subsequently integrated over time as described below.

### 2.1 Parameter selection

The parameters of the DPD model were selected based on a recently developed fine-tuned mapping of the DPD parameters to SI units derived from atomistic nonequilibrium molecular dynamics (NEMD) simulations of polyethylene melts modeled using the Siepmann-Karaborni-Smit (SKS) united-atom model<sup>54</sup>. Each DPD particle was taken to represent 3 methylene groups of the united-atom model PE chain. The mass of each DPD particle was set to unity,  $m = 1$ , as was the force cutoff distance,  $r_c = 1$ , and the temperature,  $k_B T = 1$ , which are commensurate with universally accepted parameters. Consequently, the DPD time scale unit was defined as  $\tau_{DPD} = (mr_c^2/k_B T)^{0.5}$ . Furthermore, in order to avoid temporal divergence of the simulations due to large temperature fluctuations, the coefficient of viscous friction was fixed at  $\gamma^D = 4.5$ <sup>58</sup>. The remaining system specific parameters are summarised in Table 1.

As mentioned above, the DPD model used in these simulations has previously been mapped onto NEMD simulations employing the SKS united-atom model of PE, which demonstrated that DPD accurately predicted structural and rheological properties under transient and steady-state flow conditions in both steady-state and startup shear and planar elongational flows<sup>54,59</sup>. Moreover, this study introduced a universal methodology for

Table 1 DPD simulation parameters used in this work. These parameters were chosen systematically by comparisons with equilibrium and nonequilibrium molecular dynamics simulations of atomistic polyethylene liquids<sup>54</sup>.

Parameter	Value	Units
$a$	200	$k_B T / r_c$
$\gamma^D$	4.5	$(mk_B T / r_c^2)^{1/2}$
$r_{eq}$	0.95	$r_c$
$\Delta t$	0.012	$(mr_c^2 / k_B T)^{1/2}$
$\rho$	1	$m / r_c^3$
$k_{bend}$	2.38	$k_B T$
$k_{spr}$	400	$k_B T / r_c^2$

Table 2 Dimensions of the simulation cells for each melt.  $L_x$ ,  $L_y$ , and  $L_z$  are displayed as multiples of the equilibrium value of  $R_g$  ( $\equiv \langle R_g^2 \rangle^{0.5}$ ) and also in dimensionless  $r_c$  units (displayed within parentheses). The total number of DPD particles used in the respective simulations are also tabulated.

Chain Length	$L_x$	$L_y$	$L_z$	$N_p$
N-250	$11R_g$ (160)	$4R_g$ (58)	$2R_g$ (31)	291,000
N-400	$15R_g$ (200)	$4R_g$ (60)	$2R_g$ (32)	409,200
N-1000	$6R_g$ (127)	$4R_g$ (84)	$1.5R_g$ (30)	320,000
( $Wi \leq 60$ )				
N-1000	$17R_g$ (351)	$4R_g$ (84)	$1.5R_g$ (30)	886,000
( $Wi \geq 80$ )				

converting primitive physical properties (*i.e.*, mass, time, and length) from DPD units to SI units<sup>54</sup>. In the derived method, the paired DPD/NEMD chains with matching characteristics, such as entanglement number, segmental mean-squared-displacement at equilibrium, chain end-to-end probability distribution function, and zero-shear viscosity, were observed to closely match each other under a full range of strain rates in both shear and elongational flows. The following scaling factors were calculated for converting properties based on DPD units to SI units: (1)  $F_l = 4.238 \text{ \AA} / l_{DPD}$ , (2)  $F_t = 1.05 \times 10^{-3} \text{ ns} / t_{DPD}$ , and (3)  $F_v = 4.515 \times 10^{-5} \text{ Pa s} / \eta_{DPD}$ .

Equilibrium and nonequilibrium DPD simulations of linear PE melts were performed in the canonical ( $NVT$ ) ensemble. The LAMMPS<sup>60</sup> computing platform was used to integrate Newton's equations of motions using the velocity-Verlet algorithm<sup>58</sup> with a suitably small time-step of  $\Delta t = 0.012 \tau_{DPD}$  and a reduced particle density of  $\rho = 1$ . Table 2 provides the sizes of the simulation cells at equilibrium for the three PE melts,  $C_{750}H_{1502}$  (N-250),  $C_{1200}H_{2402}$  (N-400), and  $C_{3000}H_{6002}$  (N-1000), which are modeled using coarse-grained DPD chains of bead number as indicated within the parentheses. The thermodynamic state point simulated for each melt was based on realistic PE melt density of  $0.766 \text{ g/cm}^3$  at a temperature of  $450 \text{ K}$ <sup>61</sup>. The dimensions of the simulation boxes were chosen to be sufficiently large (especially in the flow direction) to avoid self-interaction of highly stretched chains with their own periodic images at high strain rates. Furthermore, at these high strain rates, significant flow-induced disentanglement occurs along with substantial chain stretching, thereby eliminating the possibility of any network-induced box-size effect. Note that DPD is a momentum-conserving, boundary-driven simulation technique where momentum is imposed on the

particles by passing through the periodic boundary condition of the deformed simulation cells. To represent the correct entangled polymer physics and the correct scaling of entangled polymer melts, the geometric criterion of Nikunen *et al.*<sup>62</sup> was implemented; *i.e.*,  $\sqrt{2}r_{min} > l_{max}$  where  $r_{min}(=0.77)$  and  $l_{max}(=1.05)$  are the effective radius of the particles and the maximum distance between adjacent beads in the backbone, respectively. Careful selection of the force-field parameters, such as  $k_{spr} \geq 2a$ , in conjunction with this criterion is a highly effective and cost efficient method to prevent chain crossing. It should also be noted that  $r_{min}$  and  $l_{max}$  are the minimum and maximum distances between particles based on the pair correlation function,  $g(r)$ , and probability density function of bond length,  $P(r_{eq})$ . More details regarding the DPD tuning parameters can be found in previous publications.<sup>37,41,54,62</sup>

The stress tensor,  $\mathbf{T}$ , was calculated over all particles within the simulation cell, and on some occasions, over particles in selected layers of the simulation cell to generate a stress profile within the flowing system. The total stress was calculated according to the Irving-Kirkwood equation<sup>63</sup>,

$$\mathbf{T} = \frac{N_p k_B T}{V} \delta + \frac{\langle \sum_{i=1}^{N_p} \mathbf{r}_i \mathbf{F}_i^{tot} \rangle}{3V}, \quad (6)$$

where the first term quantifies the hydrodynamic pressure and the second term represents the extra stress associated with viscoelastic effects.

## 3 Results and Discussion

### 3.1 Quiescent properties

The physical properties of the three PE melts in the quiescent equilibrium state were calculated from DPD simulations; selected results are summarized in Table 3. The ensemble averaged mean-squared end-to-end distance,  $\langle R^2 \rangle^{1/2}$ , and the ensemble averaged radius of gyration,  $\langle R_g^2 \rangle^{1/2}$ , were extracted from conformational analysis. Moreover, the Kuhn segment length,  $b$ , and the number of Kuhn segments,  $N_K$ , were calculated using standard theory as  $b = \langle R^2 \rangle / L_{max}$  and  $N_K = \langle R^2 \rangle / b^2$ , where  $L_{max}$  is the contour length of the PE chains. The  $L_{max}$  were calculated as 237.5, 380, and 949.5 in dimensionless DPD units for the N-250, N-400, and N-1000 melts, respectively. The disengagement time of the entangled PE melts at equilibrium,  $\tau_d$ , was obtained by fitting a sum of two or three term exponential functions to the ensemble-averaged auto-correlation function as  $\langle \mathbf{u}(\tau) \cdot \mathbf{u}(t + \tau) \rangle = \sum c_i \exp(-2\pi t / \tau_i)$ <sup>52</sup>, where  $\mathbf{u} = \mathbf{R} / |\mathbf{R}|$  is the unit end-to-end vector and the  $c_i$  are fitting parameters. This method was proven accurate in earlier NEMD investigations of atomic PE melts<sup>46,48,49</sup>, and it was shown to be consistent with reptation-based calculation of the disengagement time,  $\langle \mathbf{R}(0) \cdot \mathbf{R}(t) \rangle = \sum_{p:odd} \frac{8}{p^2 \pi^2} \exp(-p^2 t / \tau_d)$ <sup>20,64</sup>. Similarly, the longest characteristic (decorrelation) time of the chains under flow,  $\tau_{d_f}$ , and characteristic rotation time scale,  $\tau_{r_f}$ , were calculated via the expression  $\langle \mathbf{u}(\tau) \cdot \mathbf{u}(t + \tau) \rangle = c \exp(-2\pi t / \tau_{d_f}) \cos(-2\pi t / \tau_{r_f})$ , where  $c$  is a fitting parameter.

The computed disengagement times of the three melts reveal the expected scaling of  $\tau_d \propto N^{3.3}$  at the values of  $N$  examined

Table 3 Equilibrium properties of the simulated PE melts. Entries are displayed in both DPD units (upper numbers) and physical units (lower numbers), where applicable.

DPD Chain	$\langle R^2 \rangle^{0.5}$	$\langle R_g^2 \rangle^{0.5}$	$\tau_d$	$\tau_R$	$Z_k$	$Z$	$N_K$
N-250	29.7	12.17	$1.35 \times 10^6$	$4.35 \times 10^4$	18.5	10.4	62
	125.65 Å	51.57 Å	$1.42 \pm 0.01 \mu s$	$0.0457 \mu s$			
N-400	38.4	15.50	$6.57 \times 10^6$	$1.30 \times 10^5$	29.1	16.7	100
	162.73 Å	52.97 Å	$6.89 \pm 0.01 \mu s$	$0.136 \mu s$			
N-1000	61.1	24.99	$1.30 \times 10^8$	$1.14 \times 10^6$	73.0	38.0	242
	258.95 Å	105.91 Å	$136.5 \pm 0.1 \mu s$	$1.2 \mu s$			

herein. Moreover, the characteristic Rouse time,  $\tau_R$ , and characteristic entanglement time scale,  $\tau_e$ , were determined based on the Doi-Edwards<sup>20,64</sup> tube model as  $\tau_R \equiv \tau_d/3Z$ , and  $\tau_e \propto \tau_R/Z^2$ , where  $Z$  is the ensemble average number of entanglements per chain at equilibrium. Theoretically, one can calculate the equilibrium chain entanglement number by  $Z = \langle L \rangle / a_t = N_K b^2 / a_t^2 = \langle L \rangle^2 / \langle R^2 \rangle$ , where  $\langle L \rangle$  and  $a_t$  are the average primitive chain contour length and the tube diameter at equilibrium, respectively. The entanglement network topological analysis using the Z1-code of Kröger<sup>65–68</sup> provides the  $L$  and  $a_t$  for calculation of  $Z$ . Moreover, the Z1-code introduces an alternative topological quantifier, the number of kinks per chain,  $Z_k$ . At equilibrium  $Z_k/Z \approx 2^{46,48,49,66,69,70}$ ; however, it is not clear if this ratio remains the same under nonequilibrium flow conditions. It is also not clear if the physical definitions of  $Z$  and  $a_t$  remain valid under nonequilibrium conditions. Therefore, in the following,  $Z_k$  is used as the indicator of entanglements under nonequilibrium flow conditions since it is directly calculated by the Z1 code via an unambiguous algorithm.

## 3.2 Steady-state shear flow

### 3.2.1 Steady-state simulation overview

The unidirectional step-strain startup shear flow virtual experiments were performed over a wide range of shear rates by application of a particular strain rate at  $t = 0$  and evolving the system in time until steady-state was attained. The simulations were then continued at steady-state for a sufficiently long time period to allow statistically meaningful calculations of steady-state rheological and topological system properties. Within the simulation box,  $x$  is the flow direction,  $y$  is the flow gradient direction, and  $z$  is the neutral direction. The bulk shear rate is defined based on the applied linear velocity profile at  $t = 0$ . The three PE melts were subjected to shear rates quantified in terms of the Weissenberg number, *i.e.*,  $Wi = \tau_d \dot{\gamma}$ , where  $\dot{\gamma}$  is shear rate, over the ranges  $1 \leq Wi \leq 500$ ,  $1 \leq Wi \leq 10,000$ , and  $1 \leq Wi \leq 80,000$  for the N-250, N-400, and N-1000 PE melts, respectively. Note that the initial ( $t = 0$ ) system configurations corresponded to a quiescent equilibrated state for each melt.

The steady-state properties of the PE melts under shear flow were extracted from simulation data, including conformational characteristics (*e.g.*,  $\langle R^2 \rangle^{1/2}$ ,  $\langle R_g^2 \rangle^{1/2}$ , and tube segmental orientation tensor,  $\mathbf{S} = \langle \mathbf{u}_{seg} \mathbf{u}_{seg} \rangle$ ), shear stress ( $\sigma_{xy}$ ), viscosity ( $\eta = \sigma_{xy}/\dot{\gamma}$ ), and normal stress differences ( $N_1 = \sigma_{xx} - \sigma_{yy}$ ,  $N_2 = \sigma_{yy} - \sigma_{zz}$ ). Bulk steady-state properties were calculated throughout

the simulated system (in the following subsection; band-specific properties will be discussed later) whether or not shear-banding was evident. Note that the orientation tensor  $\mathbf{S}$  is based on the ( $\mathbf{u}_{seg}$ ) unit vector spanning the distance from one end of a chain segment to the other, with the length of the segment determined by  $Z_k/2$  at any value of  $Wi$ . At equilibrium,  $Z \approx Z_k/2$ , so the tube segments correspond to the entanglement length; however, at nonzero  $Wi$ ,  $Z$  is essentially undefined, or at least not well understood, so  $Z_k/2$  is used since  $Z_k$  is unambiguously defined by the Z1 code.

### 3.2.2 Rheology and flow-induced network topology

The steady-state rheological and topological properties for all the PE melts examined herein are qualitatively very similar. Overall, the steady-state shear properties of the entangled melts exhibit four distinct regions of dynamical response, based on their characteristic time scales,  $\dot{\gamma} < \tau_d^{-1}$ ,  $\tau_d^{-1} < \dot{\gamma} < \tau_R^{-1}$ ,  $\tau_R^{-1} < \dot{\gamma} < \tau_e^{-1}$ , and  $\tau_e^{-1} < \dot{\gamma}$ <sup>46,48,49</sup>. The limits of these ranges are indicated in Figure 1(c) for each of the PE melts, although  $\tau_d^{-1}$  is not indicated since it occurs at  $Wi = 1$  for all melts. Other than  $Wi = 1$ , the range limits expressed as shear rates correspond to different  $Wi$  for each melt, as indicated in the figure.

Within the linear viscoelastic flow regime,  $\dot{\gamma} < \tau_d^{-1}$  or  $Wi < 1$ , the characteristic flow time scale is larger than  $\tau_d$ , and therefore the polymer chains are able to relax faster than the flow can impose individual molecular stretching. Consequently, in this flow regime, the primary rheological response is caused by a slow re-orientation of the tube network, as quantified by  $S_{xy}$ , which increases substantially from its quiescent null value as the average orientation angle decreases precipitously from its zero shear limit of  $45^\circ$ , as displayed in Figure 1. The quantity  $S_{xx} - S_{yy}$  remains fairly low since there is no substantial chain stretching in this flow regime (Fig. 3(b)). The steady-state shear stress,  $\sigma_{xy}$ , which is proportional to  $S_{xy}$ , increases linearly with  $Wi$  in this flow regime, producing a shear viscosity that remains close to its zero-shear Newtonian limit, as observed in Figure 2. Likewise, the first normal stress difference, which is proportional to  $S_{xx} - S_{yy}$ , remains vanishingly small due to the lack of chain stretching (Fig 2(c)). No shear banding is observed within the linear viscoelastic regime for any of the three melts, as indicated by the shaded region (I) in Fig. 2(a), simply because the chain dynamics are fast enough to remain essentially equilibrated at the relatively long time scale of the flow. This statement can be verified by focusing on the microstructure of the liquids. Figure 3 indicates that the network topology is practically unchanged relative to the quiescent mi-

crostructure within the linear viscoelastic regime, in terms of both segmental stretching and average number of entanglements. Furthermore, the probability distribution function (PDF),  $P(\chi)$ , of the mean relative extension of the polymer chains,  $\chi = |\mathbf{R}|/|\mathbf{R}|_{\max}$ , remains close to the corresponding quiescent PDF for each of the three melts, which has decidedly Gaussian characteristics, as displayed in Figure 4. All of these results are consistent with most theoretical models of polymer dynamics at low shear rates.

The second flow regime exists within the shear rate range of  $\tau_d^{-1} < \dot{\gamma} < \tau_R^{-1}$ . This shear rate range corresponds to  $1 < Wi < 30, 50, 160$  for the N-250, N-400, and N-1000 melts, respectively. Both the tube orientation component  $S_{xy}$  and the shear stress  $\sigma_{xy}$  display nonmonotonic behavior in this regime. They each increase from  $Wi = 1$  up to  $Wi \approx 10$  for each PE melt, and then decrease after attaining a maximum at  $Wi$  in the range of 5-10. The tube segments begin to stretch mildly and the molecular entanglement network begins to relax as flow strength increases (Fig. 3); however, the dominant relaxation mechanism in

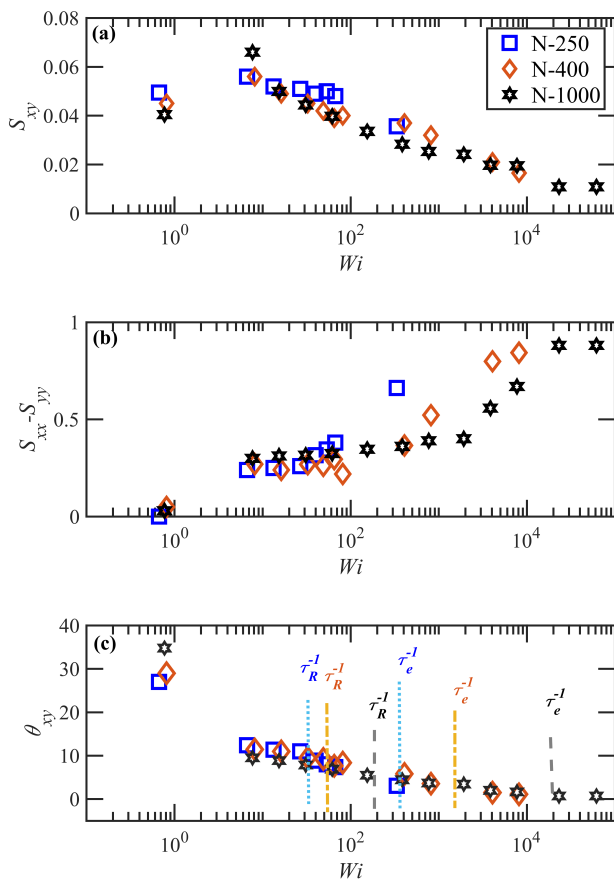


Fig. 1 Tube orientation tensor components of  $\mathbf{S} = \langle \mathbf{u}_{seg} \mathbf{u}_{seg} \rangle$ , where  $\mathbf{u}_{seg}$  is the unit vector based on the segmental end-to-end vector, vs.  $Wi$ : (a)  $S_{xy}$ , (b)  $S_{xx} - S_{yy}$ , and (c)  $\theta_{xy}$ , the average angle of tube segment orientation, defined as the angle between the eigenvector associated with the largest eigenvalue of  $\mathbf{S}$  and the flow direction in the  $xy$ -plane.

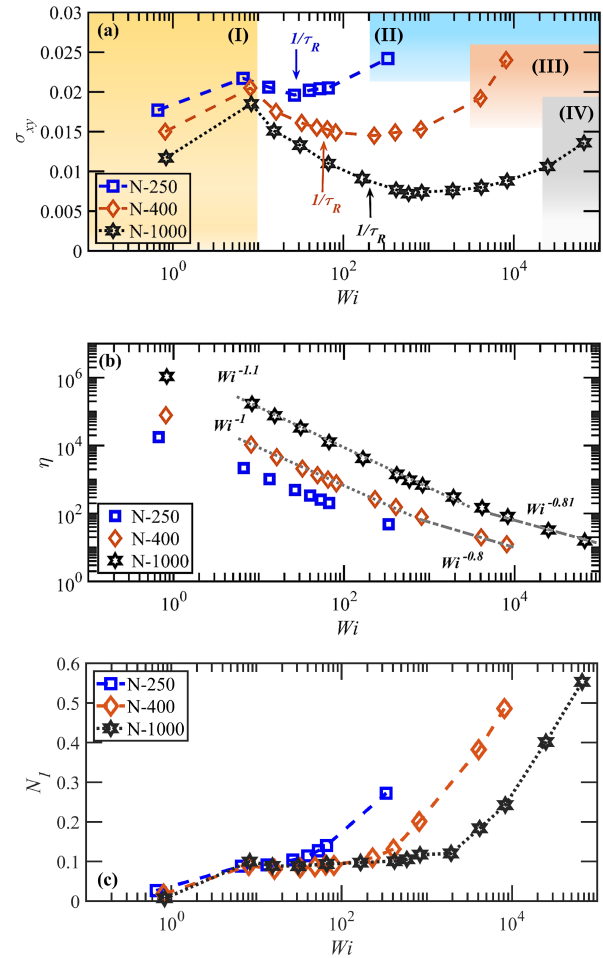


Fig. 2 Steady-state bulk rheological behavior of the three PE melts, N-250, N-400, and N-1000: (a) steady-state shear stress profile ( $\sigma_{xy}$  vs.  $Wi = \dot{\gamma}\tau_d$ ) in DPD units; (b) steady-state viscosity profile ( $\eta$  vs.  $Wi$ ) in DPD units; and (c) steady-state first normal stress difference profile ( $N_1$  vs.  $Wi$ ) in DPD units. The shaded regions in Panel (a) indicated the absence of shear banding: Region I, no shear banding (NSB), Region II, NSB for the N-250 melt, Region III, NSB for N-400, and Region IV, NSB for N-1000. Note that Region I ends at  $Wi \approx 10$  for all melts and that Regions II, III, and IV begin at approximately  $\dot{\gamma} = \tau_e^{-1}$  for the three melts. Within the non-shaded region between  $Wi \approx 10$  and  $\dot{\gamma} = \tau_e^{-1}$  for each melt, one can observe both steady and transient shear banding, as well as reverse flow. The viscosity shear-thinning exponents for the two shear rate regions  $\tau_d^{-1} < \dot{\gamma} < \tau_e^{-1}$  and  $\dot{\gamma} > \tau_e^{-1}$  are noted in the plot of Panel (b). Error bars on stress values are smaller than the size of the symbols in all cases, and are therefore omitted.

this region remains the orientation of the tube segments, which continues its precipitous drop. The number of entanglements experiences a gradual decline from its quiescent value. No shear banding is observed at  $Wi < 10$ , but the shear viscosity begins to exhibit a characteristic shear-thinning behavior quantified by a power-law coefficient of  $-1$ , as displayed in Fig. 2(b). The first normal stress difference in the range  $1 \leq Wi \leq 10$  begins to rise substantially, effectively tracking the increase in  $S_{xx} - S_{yy}$ .

Once past the maximum in  $S_{xy}$  at  $Wi \approx 5-10$ , a number of interesting dynamic phenomena begin to appear in the shear rate

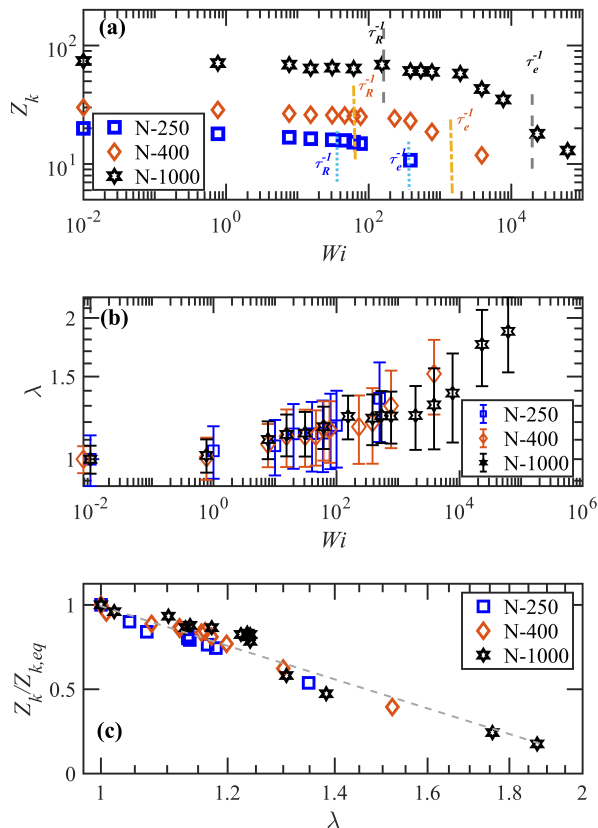


Fig. 3 The topological network characteristics: (a) average number of kink entanglements per chain  $Z_k$  vs.  $Wi$ ; (b) average tube stretch  $\lambda$  vs.  $Wi$ ; (c) normalized entanglements per chain  $Z_k/Z_{k,eq}$  vs. tube stretch  $\lambda$  under steady-state conditions for the N-250, N-400, and N-1000 PE liquids. Note that the equilibrium properties are reported at  $Wi = 0.01$  in Panels (a) and (b) since  $Wi = 0$  cannot be displayed on the semi-log plot.

range  $10/\tau_d < \dot{\gamma} < 1/\tau_R$ , the upper limit of which corresponds to  $Wi$  of 35, 55, and 160 for the N-250, N-400, and N-1000 melts, respectively. These phenomena are all associated with the shear-induced degradation of the entanglement network, as evidenced by the gradual but steady decrease in the entanglement number,  $Z_k$ , that is apparent in Fig. 3(a).  $Z_k$  follows a power-law decrease with  $Wi$  in this strain rate regime with an exponent of about  $-0.017$  to  $-0.03$ . As the density of topological constraints decreases, the tube segments are less constrained and begin to extend—see Fig. 3(b). In fact, the direct correlation between entanglement density and tube stretch is evident in Fig. 3(c). The increase in strength of shear forces and reduction in topological constraints at  $\dot{\gamma} > 10/\tau_d$  result in the onset of a quasiperiodic tumbling motion of the molecules at a frequency that increases with increasing shear rate.<sup>46,48,49,52,71–73</sup> During a typical rotational cycle, molecular chain ends diffuse back along the chain axis forming a hairpin-like structure aligned close to the flow direction that flips orientation as the chain ends pass the molecular center. The PDFs of mean relative extension shown in Fig. 4 at

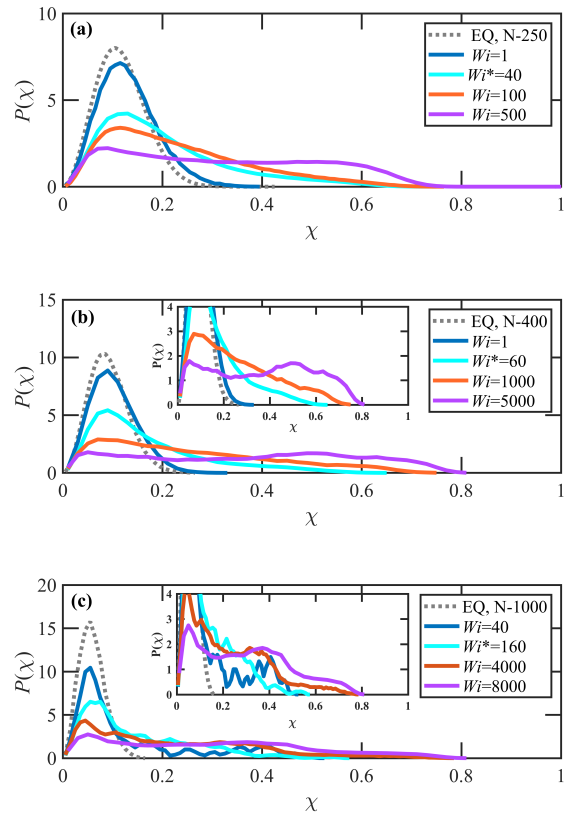


Fig. 4 Probability distribution function of chain mean relative extension,  $\chi$ , for (a) the N-250 melt, (b) the N-400 melt, and (c) the N-1000 melt subjected to steady-state shear flow at selected  $Wi$  within different flow regimes. EQ denotes the quiescent equilibrium state. The insets show critical portions of the PDFs on an expanded scale. PDFs corresponding to  $Wi$  numbers at  $\dot{\gamma} \approx \tau_R^{-1}$  for each melt are labeled with an asterisk (\*).

$Wi$  near the upper limit of this regime illustrate the broadening of the distribution that occurs with the onset of rotational molecular cycles of the individual chains, and the commensurate increase in mean relative extension that derives from the degradation of the entanglement network; *i.e.*, individual chains with few entanglements are free to stretch out significantly in the flow direction and to rotate quasiperiodically in response to the imposed vorticity field. Commensurately with this,  $S_{yy}$  decreases with increasing shear rate (Fig. 1(a)), also because of the broadening of its PDF that occurs with the onset of chain tumbling, whereas  $S_{xx} - S_{yy}$  attains a wide plateau (Fig. 1(b)) that is echoed in the plot of  $N_1$  (Fig. 2(c)). This cyclical rotation of the chain molecules effectively reduces their average degree of orientation,  $\theta_{xy}$ , and narrows the orientation angle distribution (not shown). The precipitous decrease in average orientation angle that occurred at lower  $Wi$  flattens out into a gradually descending plateau at about  $10^\circ$  with respect to the flow direction for all PE melts—see Fig. 1(c).

For shear rates in the range of  $10\tau_d^{-1}$  ( $Wi = 10$ ) to  $\tau_R^{-1}$ , shear stress decreases with increasing shear rate (Fig. 2(a)), attain-

ing a minimum in the vicinity of  $\tau_R^{-1}$ . As demonstrated previously, the nonmonotonicity of the shear stress profile is closely related to the monodispersity of the sample. For a polydisperse melt, prior simulations have demonstrated that the degree of nonmonotonicity is related to the polydispersity index: as the melt becomes more polydisperse, the nonmonotonic stress region becomes a plateau region<sup>41</sup>. This is because the wide range of characteristic time scales available to a system of varying molecular length effectively smears the distinct transitions in dynamical behavior observed in monodisperse liquids over a wider range of  $Wi$ ; *i.e.*, shorter chains experience a critical  $Wi$  transition at a significantly larger shear rate than longer chains. Hence for polydisperse melts, one observes a shear stress plateau at intermediate shear rates rather than the nonmonotonicity observed herein for monodisperse melts<sup>41</sup>. In the monodisperse simulations, the onset of the destruction of the entanglement network and subsequent tumbling dynamics of the molecular chains is responsible for this decrease in shear stress. The result is a shear-thinning viscosity that scales with a power-law index of approximately  $-1$  (Fig. 2(b)). Note that shear banding is observed throughout the  $Wi$  region where the shear stress is decreasing with increasing strain rate; this phenomenon will be discussed separately below.

At approximately  $\dot{\gamma} \approx \tau_R^{-1}$  for each melt, the shear stress attains a minimum with respect to  $Wi$ , followed by a substantial increase in shear rate as the third shear rate regime is entered; *i.e.*,  $\tau_R^{-1} < \dot{\gamma} < \tau_e^{-1}$ . Note that  $\tau_e^{-1}$  corresponds to  $Wi$  of about 400, 1,500, and 21,000 for the N-250, N-400, and N-1000 PE melts, respectively, as denoted in Figs. 1(c) and 2(a). In this strain rate regime, the transition of the dominant relaxational mechanism from segmental orientation to tube stretching occurs along with an acceleration in the destruction of the entanglement network, which is observed as an increase in the magnitude of the power-law index of the  $Z_k$  scaling ranging from  $-0.034$  to  $-0.12$  for the three melts. This phenomenon manifests itself in the various physical properties of the flowing liquid. Although the individual chains may be rotating at higher frequencies than at lower shear rates, they are doing so by assuming more stretched hairpin configurations. In this strain rate regime, however, one cannot fully understand the steady-state behavior without recognizing the influence of steady-state shear banding on the bulk system physical properties.

As described in detail in a subsequent section, within the nonshaded  $Wi$  region shown in Fig. 2(a), the flow cell segregates into two (or more) regions with different apparent shear rates, one corresponding to a relatively fast band at a higher shear rate, and another slow band at a lower shear rate. Bulk system properties within the non-shaded regime are thus an average over the property values within each band. As an example, for the N-1000 melt at nominal  $Wi = 4,000$ , startup of shear flow ultimately generates two distinct shear bands, a fast band at  $Wi_{fast} \approx 4,000$  and a slow band in which  $Wi_{slow}$  is much smaller than the nominally imposed shear rate. Within these bands,  $S_{xy,slow} = 0.04$  and  $S_{xy,fast} = 0.016$ , whereas the bulk average over the entire flow cell is  $S_{xy} = 0.02$ . Likewise, bulk average first normal stress difference is calculated as  $N_1 = 0.19$ , whereas  $N_{1,slow} = 0.1$  and  $N_{1,fast} = 0.27$  (see Fig. 5(b)). Similarly,  $Z_{k,slow} = 56$  and  $Z_{k,fast} = 20$  with overall

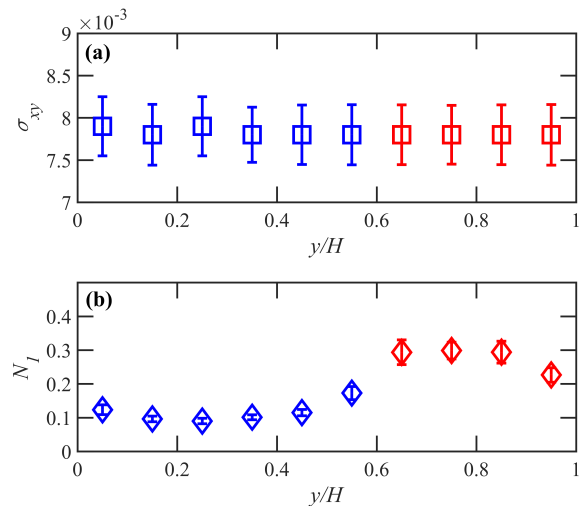


Fig. 5 (a) Average induced shear stress and (b) average induced first normal stress difference for the N-1000 melt at  $Wi = 4,000$  at various layers spanning the  $y$ -direction. The color of data points indicate layers within the fast (red) and slow (blue) shear band regions.

$Z_k = 43$ , and  $\lambda_{slow} = 1.14$  and  $\lambda_{fast} = 1.52$  with overall  $\lambda = 1.3$ . Note, however, that the shear stress is constant throughout both bands of the simulation cell at  $\sigma_{xy} = 0.0078$ , as illustrated in Figure 5(a). Since the bands have different shear rates, the viscosity is proportionally different between the two bands. This appears to be a universal feature of the shear bands formed throughout the simulations; *i.e.*, the flow segregates into shear bands of disparate shear rates while maintaining a constant shear stress throughout the simulation cell. Hence the formation of steady-state shear bands is a result of the flow kinematics acting on the collective microstructure of localized regions of molecular chains. [Such flow-induced microstructural inhomogeneities have recently been observed in elongational flows of polyethylene melts and solutions in both atomistic nonequilibrium molecular dynamics and DPD simulations<sup>50,59,74–78</sup>, which also exhibited constant stress profiles in spite of the induced inhomogeneities.] These chains exhibit a wide array of individualism in their responses to the imposed kinematics (as discussed in detail below), which creates the requisite flow-induced instability necessary to generate distinct bands of vastly different inherent microstructure and local shear rate.

Within the range of  $\tau_R^{-1} < \dot{\gamma} < \tau_e^{-1}$ , the microstructural and topological properties of the melts begin to change dramatically with increasing shear rate. The large changes in these properties are primarily driven by the dynamics of the fast band rather than the slow band. The orientation angle continues to flatten out toward the flow direction, as does  $S_{xy}$ , indicating the increasing degree of orientation of the stretched chain segments as they undergo quasiperiodic tumbling cycles (Fig. 1(a), (c)). The stretching of chain segments is captured by the steady increase in both  $S_{xx} - S_{yy}$  (Fig. 1(b)) and  $\lambda$  (Fig. 3(b)), with a commensurate steady and accelerating decline in the entanglement density,  $Z_k$  (Fig. 3(a)). The overall shear stress attains a minimum near  $\tau_R^{-1}$  and climbs with increasing  $Wi$  thereafter through  $\tau_e^{-1}$ . This

is driven by the nominal applied strain rate which determines the constant shear stress applied throughout the simulation cell, as illustrated in Fig. 5(a). As the applied shear rate increases, the shear stress thus grows within both bands commensurately. The shear viscosity continues to display a power-law behavior with index of approximately  $-1$ . The first normal stress difference gradually begins to increase with applied  $Wi$ , mirroring the trends observed for  $S_{xx} - S_{yy}$  and  $\lambda$ , although this growth is primarily due to the fast band (Fig. 5(b)). The PDFs of mean relative extension continue to broaden (Fig. 4), indicating the rotational motion of the molecules in the fast band, and as  $\dot{\gamma} \rightarrow \tau_e^{-1}$  a bimodal distribution becomes evident. A low  $\chi$  peak is observed that is associated with chains within the slow band as well as those within the fast band that are instantaneously in configurations with low  $\chi$  values. There is also a high  $\chi$  peak associated with the chains within the fast band that are highly stretched and oriented along the flow direction typically at the apex of their tumbling cycles. The broad distribution of chains between these two peaks largely stems from the quasiperiodic change in  $\chi$  values of the rotating molecules of the fast band. All of this behavior is consistent with atomistic nonequilibrium molecular dynamics simulations of polyethylene melts under shear flow<sup>46,48,49</sup>. Throughout much of the range  $\tau_R^{-1} < \dot{\gamma} < \tau_e^{-1}$ , one can observe steady-state shear band formation, but as  $\dot{\gamma} \rightarrow \tau_e^{-1}$  only transient shear banding is observed where distinct bands form temporarily during startup of shear flow but then dissipate into bulk flow with a uniform linear velocity profile across the entire simulation cell.

At  $\dot{\gamma} > \tau_e^{-1}$ , no transient or steady-state shear banding is observed for any of the three PE melts. Evidently, at these strong strain rates, the dynamics evolve directly into a homogeneous, uniform system that spans the entire simulation cell with a uniform linear velocity profile. In this shear rate region, the flow time scale is faster than the time scale on which the molecules experience tube constraints, and furthermore, the entanglement density plunges and segmental stretching grows substantially. As the chain segments stretch out, they become increasingly aligned along the flow direction (Fig. 1(c)). The molecular chains rotate freely with the destruction of the entanglement network in much the same way as chain-like molecules dissolved in dilute solution. For individual chains, the surrounding chains serve as the solvent, behaving similarly to a low molecular weight solvent since the number of entanglements is minimal. As such, the time scale of the flow is governed by the vorticity of the kinematics, and the decorrelation time  $\tau_{d_f}$  becomes indistinguishable from the rotational time scale,  $\tau_{r_f}$ , which is imposed by the flow vorticity. Shear stress and first normal stress difference rise significantly since there are no longer any counterbalancing forces: any increase in shear rate simply results in an augmentation of the presiding dynamics, such as an increase in segmental stretching and frequency of dynamic chain rotation. The shear viscosity power-law index in this  $\dot{\gamma}$  region drops to  $-0.8$ , consistently with results of prior atomistic nonequilibrium molecular dynamics of PE melts<sup>46,48,49,53</sup>. PDFs of mean relative extension (Fig. 4) display the broad, bimodal profiles exhibiting peaks at both very low and very high relative extensions, which is also a signature of the tumbling dynamics evident at high  $Wi$ <sup>46,48,49,53</sup>.

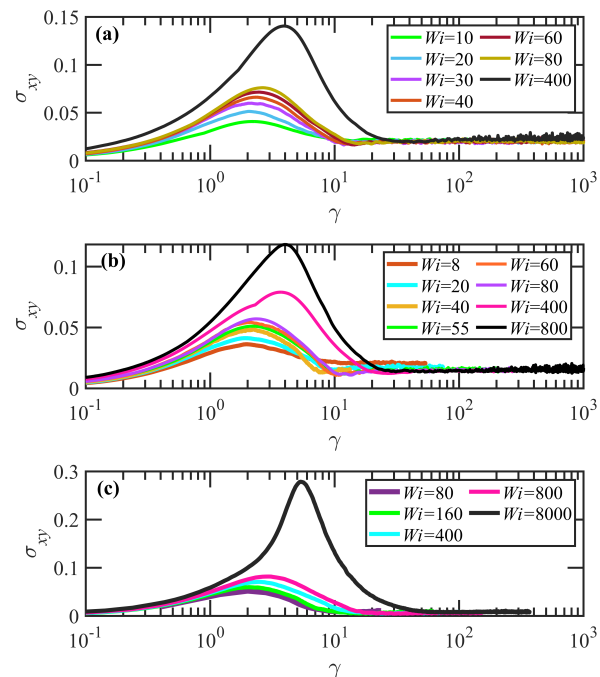


Fig. 6 Startup shear stress evolution as a function of applied shear strain at various  $Wi$ : (a) N-250 melt, (b) N-400 melt, and (c) N-1000 melt.

### 3.3 Transient shear flow

#### 3.3.1 Startup shear flow behavior and microstructural evolution

The startup shear simulations are implemented by applying a specific value of shear rate at  $t = 0$  to the simulation cell containing and instantaneous equilibrated configuration of a particular PE melt, as described in Table 2. Various rheological and topological properties are tracked as functions of time, which can be represented in dimensionless strain units,  $\gamma = \dot{\gamma}t$ . Plots of the temporal evolution of shear stress versus strain are displayed in Figure 6 for the three PE melts at various values of applied  $Wi$ . In agreement with reptation theory, the maximum of the stress overshoot occurs at approximately two strain units ( $\gamma \approx 2$ ) for all three monodisperse, linear PE melts in the range of  $\dot{\gamma} < \tau_R^{-1}$ . At higher flow rates,  $\tau_R^{-1} < \dot{\gamma} < \tau_e^{-1}$ , the position of the maximum stress overshoot gradually increases up to  $\gamma \approx 3$ , and then at  $\dot{\gamma} > \tau_e^{-1}$ , it attains a maximum strain value of  $\gamma \approx 4-5$  for all melts. Within the range  $\tau_R^{-1} < \dot{\gamma} < \tau_e^{-1}$ , an undershoot is also generally observed immediately following the overshoot, which appears to be controlled by the segmental orientation, as quantified by  $S_{xy}$ <sup>46</sup>. Indeed, the entire shear stress vs. time profile tracks closely the corresponding time evolution of  $S_{xy}$ <sup>46</sup>. Note that in all cases, the shear stress attains its steady-state value at about  $t = t_{d_f}$ , as noted previously<sup>41</sup>.

At  $Wi > 10$ , distinct steady-state shear bands begin to develop shortly after flow inception. In Figure 7, several key properties are displayed as functions of applied strain for the N-1000 melt at applied  $Wi$  of 4,000. In these plots, the simulation cell has

been subdivided in the  $y$ -direction into layers based on the final steady-state positions of the fast and slow shear bands. As noted in Fig. 5, the shear stress is evidently constant across the simulation cell. This fact is also apparent in Fig. 7(a), where it is also evident that the same holds true at all times; *i.e.*, the overall average shear stress and the stresses in the fast and slow bands are essentially equivalent at all strains. However, it does not appear that the shear stress, which faithfully tracks the evolution of the tube orientation component  $S_{xy}$ , is responsible for the development of the shear bands. Rather, it appears that the shear band development is generated by an elastic instability that is driven by the tube stretching, quantified by  $S_{xx} - S_{yy}$  and  $\lambda$ , the time evolution of which are faithfully tracked by the first normal stress difference,  $N_1$ <sup>46</sup>. Indeed, incipient shear banding generally occurs at approximately the maximum of  $N_1$ , typically located roughly 2-4 strain units after the maximum in the shear stress. In the present case, the maximum in  $N_1$  occurs at about 6-8 strain units, well after the maximum in the shear stress profile at  $\gamma \approx 4-5$ .

In most cases, as illustrated below, there is a brief time period in which a reverse flow (*i.e.*, flow in the opposite direction to that of the imposed velocity profile) is generated within the simulation cell in a small transition zone that temporarily appears between the slow and fast shear bands. The transition region is labeled as RF in Fig. 7, and it lasts for only approximately 20-30 strain units as the slow and fast bands evolve to their steady-state structures. As evident in Fig. 7(b), this reverse flow manifests during the period when the normal stresses of the two bands begin to diverge from each other. In particular, the molecules comprising the slow band recoil from their overstretched condition upon inception of flow, whereas the molecules comprising the fast band begin to experience the molecular stretching/tumbling cycles. Once the recoiling of the molecules in the slow band is essentially complete and the chains in the fast band begin rotating, the normal stresses in both bands gradually attain steady-state values with distinct and different values, as also observed in Fig. 5(b). This temporary, narrow transition zone between the two developing shear bands where RF occurs seems to appear when the time scale of the recoiling chains is larger than that of the imposed flow, and the RF effect is thus more prevalent for longer chains that exhibit a greater and longer entropic elastic response.

The dynamics of individual molecules in the fast and slow bands are displayed in Fig. 7(c) and (d), respectively, wherein each chain is assigned a random color and its time evolution is tracked. As evident from the figure, the dynamical behavior of chains within the two bands is radically different. Within the slow band, there is an initial fast stretching of the molecules after imposition of flow, followed by a sharp recoil and gradual decline to a steady-state probability distribution of chain extension. This is basically the flow-aligning behavior that one would expect from mean-field polymer rheological theory, with an average orientation angle with respect to the flow direction. Of particular note is the dynamical behavior within the time window where RF occurs: this is the strain period in which the retraction of the molecules within the slow band occurs from their overstretched state induced shortly after inception of flow. The dynamical behavior of the individual chains within the fast band is very different, how-

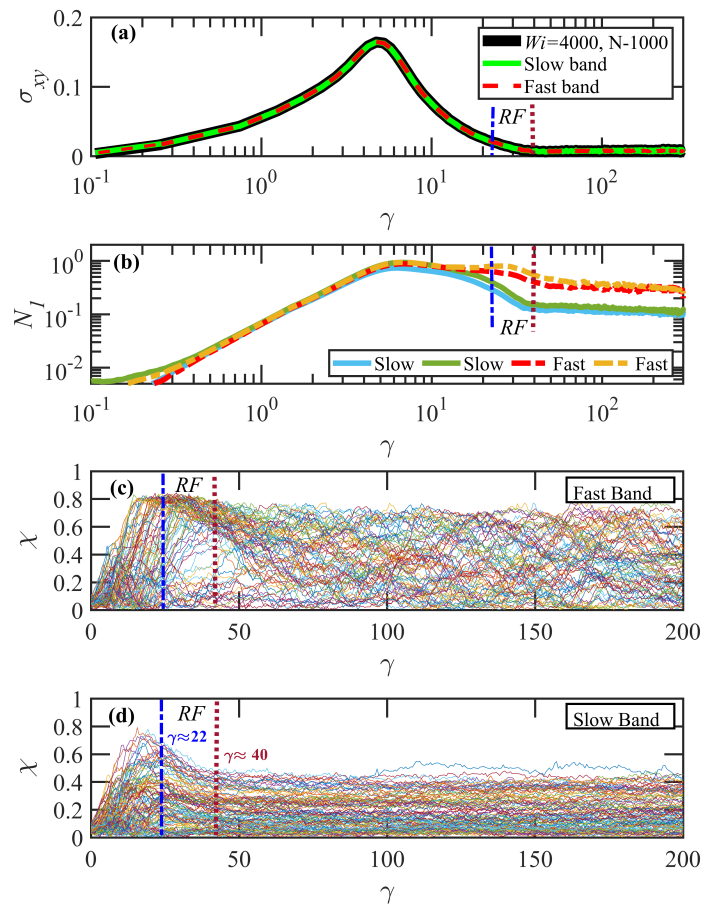


Fig. 7 (a) Temporal evolution of shear stress  $\sigma_{xy}$  vs. dimensionless strain unit  $\gamma$  for bulk flow (black line), the slow band (green line), and the fast band (dashed red line) for the  $N=1000$  liquid at  $Wi = 4,000$ ; (b) Temporal evolution of first normal stress differences  $N_1$  vs.  $\gamma$  for different layers of the slow band (solid cold color curves) and the fast band (dashed warm color curves); (c) Temporal evolution of single-chain relative extension in the fast band, where individual chains are denoted with a random color; (d) Temporal evolution of single-chain relative extension in the slow band. Note that the strain region where reverse flow is observed is identified by the dashed blue and dotted red vertical lines in each panel.

ever: the initial chain stretching after flow inception does not experience the sharp recoil observed in the slow band but rather a more gradual decline. Indeed, it appears that during the period of reverse flow, there is a transition in the fast band from highly stretched and flow-aligned individual molecules at the lower end of the strain range ( $\gamma \approx 22$ ) that evolves into a chaotic system of chains experiencing rotational cycles of stretching and contraction of the individual chain relative extension. These rotational tumbling cycles continue indefinitely, leading to the very broad PDFs at high  $Wi$  observed in Fig. 4. Reverse flow ( $22 \leq \gamma \leq 40$ ) thus appears to arise as an elastic flow instability at the interface of the fast and slow bands that is generated by the recoiling of overstretched molecules within the slow band and the relatively longer lifetime of the stretched state of the individual molecules within the fast band as they gradually develop tumbling cycles that include periods of high extension and compact contraction of relative extension.

The key physical feature of the steady-state shear-banded system is evidently the constancy of the shear stress across the bands, as depicted in Fig. 5(a). Given this observation, it is possible then to identify the bands on a stability diagram using lines of constant  $\sigma_{xy}$ , as illustrated generically in Figure 8. The overall shear stress behavior with  $Wi$  is nonmonotonic, taking the general shape of the curve in Fig. 2(a). Horizontal lines in Fig. 8 represent specific values (*i.e.*, isobars) of developed shear stress in response to flow at an imposed nominal  $Wi$ . At a shear stress of value  $\sigma_{xy}^1$ , there is only one flow state point at very low  $Wi$  where such a stress value is possible; this corresponds to steady, simple homogeneous shear flow with a uniform linear velocity profile across the simulation cell. Likewise, at a shear stress of value  $\sigma_{xy}^3$ , there is also only a single compatible flow state point, although at a very high  $Wi$  but also consistent with a smooth homogeneous linear velocity profile. However, at an applied shear stress of value  $\sigma_{xy}^2$ , a unique flow state point does not exist, and indeed, there are three flow state points that are compatible with the value  $\sigma_{xy}^2$ . In the case examined above, for the N-1000 melt undergoing steady shear flow at nominal  $Wi = 4,000$ , Fig. 5(a) indicates an average applied stress value of 0.0078. Applying this value as a horizontal line on Fig. 2(a), it is determined that the steady-state shear bands correspond to a fast band at  $Wi \approx 4,000$  and a slow band at  $Wi \approx 250$ . These two flow state points have values of associated normal stress differences  $N_1$  and average orientation angles  $\theta_{xy}$  that are quantitatively consistent with those shown in Figs. 1(a) and 2(c) at  $Wi = 250$  and 4,000, as well as the  $N_1$  profile of Fig. 5(b). The slow band thus forms at constant shear stress but at a lower value of  $N_1$ , thus relieving some of the elastic tension from the system. This appears to be the primary driving force for generation of the slow band in this case. Such behavior is consistent with shear band formation viewed as a thermodynamically driven phase transition, as discussed by Sato *et al.*<sup>79</sup> and Fielding<sup>80</sup> based on continuum models. Fig. 8 is used further in Sec. 3.3.2 to help understand the formation of shear bands under various startup conditions for the three PE melts.

### 3.3.2 Shear banding and reverse flow

Shear banding in viscoelastic melts is associated with elastic and viscous instabilities that arise as a result of a multiplicity of flow state points associated with a specific value of shear stress under startup of shear flow. Such a condition is possible because of the nonmonotonicity of the shear stress profile, and also possibly when a broad shear stress plateau is present at intermediate strain rates in the stress profile. Strain localization is primarily initiated by yielding of the entanglement network, which can be inhomogeneous in space due to the vagaries of the individual chain dynamics in local regions of the flow, which is primarily a stochastic process. Prior molecular level simulations of monodisperse and polydisperse linear PE melts have characterized the onset of shear banding and demonstrated that the local flow-induced microstructural/segmental orientation and the resulting disintegration of the entanglement network lead to strain banding instabilities<sup>41</sup>. In this study, the effect of chain length and flow strength are investigated, which highly impact the number of entanglements per chain, on the transient development of

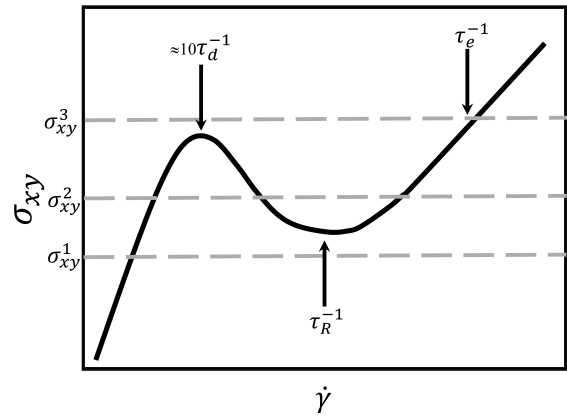


Fig. 8 Generic representation of the shear stress versus strain rate flow curve. The horizontal dashed lines denote constant values of shear stress. The intersections of these lines with the flow curve provide possible flow state points for shear banding. Vertical lines (not shown) emanating from these state points denote the strain rate of the corresponding shear band.

flow inhomogeneity for three highly entangled PE melts. Shear banding is investigated by monitoring the evolution of the velocity profile across the simulation cell over time. The profile is extracted by averaging the instantaneous velocities in the flow direction over time intervals of  $0.1\tau_{df}$  for particles within each of 20 sublayers along the gradient direction. Furthermore, the dynamical mechanisms of reverse flow are examined by detailed microstructural analysis. According to previous findings<sup>39–41</sup> and current effort, steady-state and transient shear banded structures for all three entangled melts are observed for startup shear flow with nominal shear rates within the range of  $10\tau_d^{-1} < \dot{\gamma} < \tau_e^{-1}$ . Steady-state shear banding occurs over much of this range, but only temporary transient shear banding occurs for stronger flows as  $\dot{\gamma} \rightarrow \tau_e^{-1}$ .

Figure 9(a) and (b) illustrate the evolution of shear stress versus strain for the N-250 melt at  $Wi = 30$  ( $\dot{\gamma} \approx \tau_R^{-1}$ ), and  $Wi = 80$ . The insets display the computed scaled velocity profile ( $V/V_{\max}$ ) spanned over the scaled simulation cell dimension in  $y$ -direction ( $y/H$ ) at various time instants (*i.e.*, strain units). Note that  $V_{\max}$  indicates the maximum nominal velocity at the  $y = 0$  and  $y = H$  positions, the values of which can be inferred from Table 2.

Startup of flow at  $Wi = 30$  from the stationary quiescent state (Figure 9(a)) reveals a shear stress profile with a maximum at  $\gamma \approx 2$  followed by a small undershoot at  $\gamma \approx 15$ , which is the expected behavior. At the shear stress maximum, the velocity profile is homogeneous and linear with the expected value of shear rate. However, at the maximum in the corresponding normal stress difference,  $N_1$  (not shown—see discussion in Sec. 3.3.1), which occurs at  $\gamma \approx 6$  (or  $t = 0.25\tau_{df}$ ), the onset of spatial strain-rate localization occurs with a clear separation of layer velocities with relative shear rates (*i.e.*, the slopes of the curves) that vary across the simulation cell. This separation continues to evolve until a steady-state inhomogeneous state develops consisting of two bands of roughly constant shear rates, one corresponding to

a much higher shear rate than the other. These are referred to as fast and slow bands, respectively, as illustrated in the inset of Fig. 9(a) at  $\gamma \approx 260$  ( $t \approx 9\tau_{d_f}$ ). The perturbation in the flow profile that begins at  $\gamma \approx 6$  is the manifestation of the onset of localized segmental orientation, tumbling, and entanglement network disintegration, as discussed above and illustrated further below. The cell layers comprising the slow band have an average  $N_1$  of 0.055 and an average orientation angle of  $13^\circ$ , whereas the fast band has  $N_1 = 0.188$  and  $\theta_{xy} = 6.7^\circ$ . Reading off  $Wi$  values from Figs. 1(c) and 2(c), the slow band evidently experiences  $Wi \approx 3$  and the fast band  $Wi \approx 100$ . Therefore, in reference to the generic stress profile of Fig. 8, the slow band corresponds to the lowest (left-most) flow state point and the fast band to the highest (right-most) state point—see line  $\sigma_{xy}^2$  in Fig. 8.

The behavior of the N-250 melt subjected to startup of shear flow at  $Wi = 80$  displayed in Fig. 9(b) is very similar to that at  $Wi = 30$ , except in the spatial locations of the fast and slow bands within the cell. (This aspect will be discussed thoroughly below.) However, temporary fluctuations in the shear rate and thickness

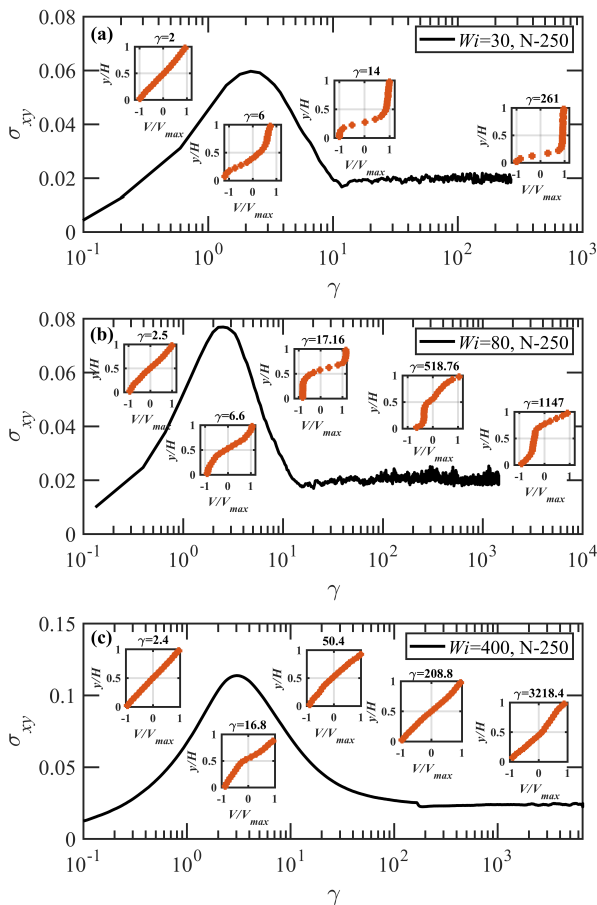


Fig. 9 The temporal evolution of shear stress vs. strain for melt N-250 undergoing startup shear flow at (a)  $Wi=30$ , (b)  $Wi=80$ , and (c)  $Wi=400$ . The insets display the scaled instantaneous velocity profiles  $V/V_{\max}$  at specific values of applied strain. Note that layer velocities are reported relative to the center of the simulation cell, such that the velocity is reported as negative in the bottom half of the cell.

of the fast and slow bands can develop and dissipate after a short period of time (compare insets at  $\gamma \approx 17$  and  $520$ ). These temporary perturbations are due to the stochastic nature of the Brownian thermal effects as implemented in the DPD simulations, which will also be addressed below. The simulation sublayers comprising the slow band have an average  $N_1$  of 0.07 and an average orientation angle of  $9^\circ$ , whereas the fast band has  $N_1 = 0.23$  and  $\theta_{xy} = 6^\circ$ . These values correspond to  $Wi$  from Figs. 1(c) and 2(c) for the slow band at  $Wi \approx 7$  and the fast band at  $Wi \approx 175$ . As in the preceding case of nominal imposed  $Wi = 30$ , at nominal  $Wi = 80$  the slow band corresponds to the lowest (left) flow state point and the fast band to the highest (right) state point of line  $\sigma_{xy}^2$  in Fig. 8.

Under startup of shear flow at high strain rates approaching  $\dot{\gamma} \rightarrow \tau_e^{-1}$ , such as at  $Wi = 400$  (Fig. 9(c)), the shear banding is only temporary in that the bands which form after the maximum in  $N_1$  dissipate into a uniform linear velocity profile with a single value of shear rate (the imposed nominal shear rate) prior to attaining a steady-state condition. This happens because as  $\dot{\gamma} \rightarrow \tau_e^{-1}$ , the steady-state shear stress is greater than the maximum value at  $Wi \approx 10$  (Fig. 2(a)), and therefore only a single steady-state flow point exists—see line  $\sigma_{xy}^3$  in Fig. 8. This is an example of what is typically referred to as ‘transient shear banding.’ The duration of transient shear banding is associated with the characteristic rotational time of the molecular chains at the applied  $Wi$ ; this aspect was discussed in prior work<sup>39,40,59</sup>.

Startup results for the N-400 PE melt are similar to those of the N-250 melt, discussed above. At  $Wi = 32$  (Fig. 10(a)), the shear stress attains a maximum at  $\gamma \approx 2$ , followed by a steep descent to a small undershoot and a gradual increase to its steady state value. Up to the shear stress maximum, the velocity profile is essentially linear with a slope that is consistent with the nominally applied shear rate. At the maximum in the first normal stress difference profile, a banded structure begins to evolve ( $\gamma = 4$ ); however, a new phenomena manifests shortly thereafter that was not evident in the N-250 melt. As shown in the inset of Fig. 10(a), in the vicinity of  $\gamma = 7$ , a narrow transition zone appears between the developing slow and fast bands where the slope of the velocity profile is actually negative, indicating flow in the reverse direction to that which was imposed. This period of time corresponds to the time period in which the individual chains in the slow band are experiencing a high degree of recoil, as evident if Fig. 7(d). After the recoiling effect dissipates, the bands gradually settle into their steady-state profiles. The slow band has an average value of  $N_1 = 0.048$  and  $\theta_{xy} = 11^\circ$ , corresponding to an effective  $Wi \approx 2$ , and the fast band has  $N_1 = 0.18$  and  $\theta_{xy} = 6.8^\circ$ , corresponding to  $Wi \approx 800$ . Thus the shear-banded system has settled into the left and right state points in Fig. 8.

The stress vs. strain profile under startup of shear flow at nominal  $Wi = 80$  for the N-400 melt is displayed in Fig. 10(b) along with the associated velocity profiles computed at specific instants in time. The overall behavior is very similar to that observed for the same melt undergoing startup of shear at  $Wi = 32$ . A reverse flow where the velocity profile assumes a negative slope is once again observed during the period in which substantial chain recoil is occurring within the slow band—see the inset at  $\gamma = 7.75$ .

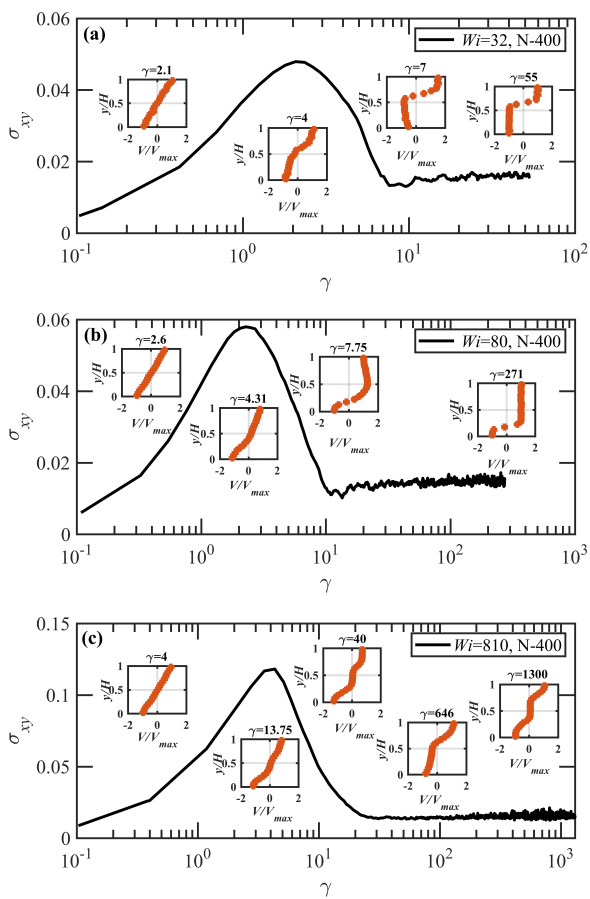


Fig. 10 The temporal evolution of shear stress vs. strain for the N-400 PE melt undergoing startup shear flow at (a)  $Wi = 32$ , (b)  $Wi = 80$ , and (c)  $Wi = 810$ . Figure insets display the evolution of the velocity profile at specific strain values.

The position of the fast band, which comprises about 20% of the width of the simulation cell in the  $y$ -direction (about  $4R_{g,yy}^{fast}$ ; *i.e.*, 4 times the  $yy$ -component of  $\mathbf{R}_g$  of chains occupying the fast band), is shifted relative to its location in the  $Wi = 32$  case, but its width is of similar dimension. The slow band has an average value of  $N_1 = 0.051$  and  $\theta_{xy} = 9.5^\circ$ , corresponding to an effective  $Wi \approx 2$ -3, and the fast band has  $N_1 = 0.195$  and  $\theta_{xy} = 6.1^\circ$ , corresponding to  $Wi \approx 800$ . Note that the nominally imposed strain rate of  $Wi = 80$  is very close to the minimum in the shear stress curve of Fig. 2(a), making a determination of shear band strain rates rather ambivalent. Nevertheless, it appears that the shear-banded system has again settled into the left and right state points in Fig. 8.

Under startup of shear flow at both  $Wi = 32$  and  $Wi = 80$  of the N-400 melt, an interesting dynamical phenomena is observed as displayed in the insets of Fig. 10(a), (b) at  $\gamma = 7$  and  $\gamma = 7.75$ , respectively, which was not observed in the behavior of the N-250 melt. In these simulations, a reverse flow is observed in which the velocity profile has a negative slope for a brief period of time in a narrow transition zone between the fast and slow bands. This indicates flow in the opposite direction to that imposed under the startup conditions. This RF is associated with the period of time

during which the molecules within the slow band are recoiling immediately after the maximum in the first normal stress difference has been attained—see Fig. 7. After the recoil is essentially complete, the velocity profile develops the characteristic banded structure of slow and fast bands with positive velocities. Presumably, this behavior was not observed in the N-250 melt because the shorter chains were insufficiently long to generate a substantial degree of recoil on the time scale of the imposed flow.

Note that assigning a specific value of shear rate to the fast and slow bands is rather ambiguous due to the limited available data and associated uncertainties in  $N_1$  and  $\theta_{xy}$ , although its order of magnitude can be established reasonably accurately. However, specific values of  $N_1$  can accurately establish the correct flow state points evident in Fig. 8 using the profile of Fig. 2(c):  $N_1 < 0.075$  generally corresponds to the left state point,  $N_1 \approx 0.1$  corresponds to the middle state point, and  $N_1 > 0.175$  corresponds to the right state point.

Startup data for the N-400 melt at  $Wi = 810$  are displayed in Fig. 10(c). The general trends in this case are mostly consistent with those at lower  $Wi$ , with the onset of shear banding being closely correlated with the maximum in  $N_1$  (not shown). In the steady-state banded structure,  $N_{1,slow} \approx 0.1$  whereas  $N_{1,fast} \approx 0.23$ , indicating that the slow band is formed at the middle state point and the fast band at the right state point. Furthermore, the fast band has grown in size to encompass roughly 40-50% of the  $y$ -dimension of the flow cell, more than double the size of the prior two  $Wi$  cases. This increase in width of the fast band might simply be related to a commensurate increase in the number of chains experiencing disentanglement and increased mobility/tumbling at the higher imposed strain rate. It is also consistent with the limited data that the width of the fast band is about 20% (roughly  $4R_{g,yy}$  of the polymer chains within the fast band) of the  $y$ -dimension of the simulation cell when the slow band is at the left state point and is 40-50% of the  $y$ -dimension when the slow band is at the middle state point. This would point to a free energy effect within the system where the balance between flow kinematics and molecular configuration is directly impacted by the particular flow state points adopted by the system. Unfortunately, there is no direct method to establish the plausibility of this hypothesis without excessive computational burden.

Figure 11(a), (b), (c) display data for startup of shear flow of the N-1000 melt at  $Wi = 160$ , 550, 4,000, respectively. The general trends mostly agree with those established for the N-250 and N-400 melts discussed above. Distinct shear bands begin to form shortly after the maximum in  $N_1$ , with RF exhibited during the period of substantial chain recoil within the slow band. At  $Wi = 160$ ,  $N_{1,slow} = 0.055$  and  $N_{1,fast} = 0.18$ , corresponding to the left and right state points, respectively. At  $Wi = 550$ ,  $N_{1,slow} = 0.066$  and  $N_{1,fast} = 0.26$ , also corresponding to the left and right state points. However, at  $Wi = 4,000$ ,  $N_{1,slow} = 0.10$  and  $N_{1,fast} = 0.27$ , corresponding to the middle and right state points—see Fig. 5. At the lowest two  $Wi$ , the fast bands occupy about 20% of the  $y$ -dimension of the flow cell, whereas at  $Wi = 4,000$ , the fast band spans 40-50% of the flow cell, consistent with results of the N-400 melt. Note that the widths of the shear bands present in the N-1000 melt are wider in actual dimension than those of the N-400

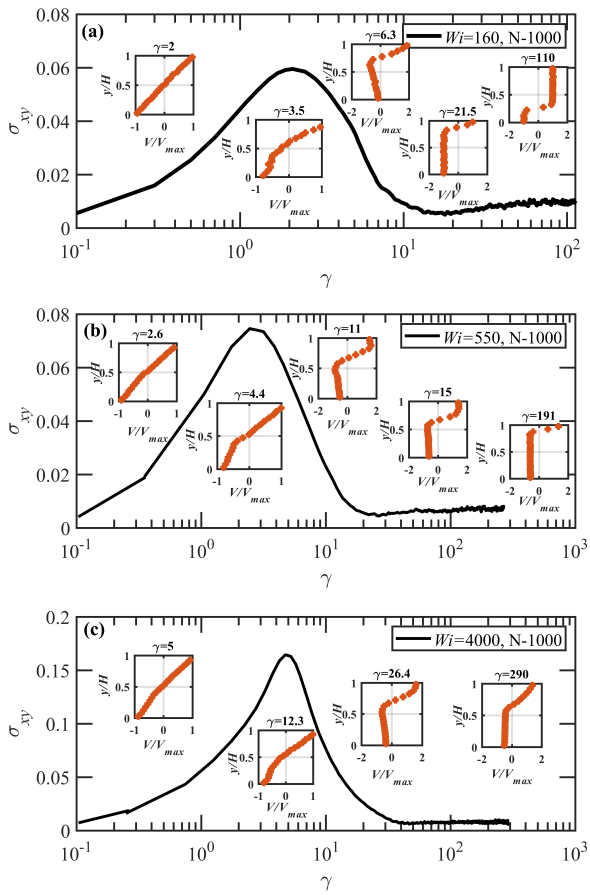


Fig. 11 The temporal evolution of shear stress vs. strain units for melt N-1000 undergoing startup shear flow at (a)  $Wi = 160$ , (b)  $Wi = 550$ , and (c)  $Wi = 4,000$ . Figure insets display the evolution of the velocity profile at specific strain units.

melt, but they still follow the general trend that the magnitude of  $R_{g,yy}$  in the fast band tends (at least at the lowest two strain rates displayed in the figure) to correspond to about 5% (i.e.,  $0.05H$ ) of the  $y$ -dimension of the flow cell. Furthermore, reverse flow is observed in all three cases, even at the highest  $Wi$  (4,000), contrary to the N-400 melt, even though the slow band occupies the middle state point at this value of  $Wi$ . It is possible that the much longer chains of the N-1000 melt might experience enough recoil at this middle state point to exhibit the RF effect, even though the nominal applied shear rate is much higher than expected relative to the N-400 melt.

A couple of points need to be made here regarding the apparent widths and spatial locations of the steady-state shear bands. First, the effect of simulation box size on the width of steady-state shear bands was examined in a preceding study<sup>39–41</sup>, where it was noted that doubling the  $y$ -dimension of the simulation cell resulted in shear bands of the same width as the original simulation, although multiple slow and fast bands were formed within the cell. Thus it is assumed that no box-size effect is present in the reported simulations. Second, the width of the shear bands and the induced local velocity profile do not appear to be affected by

running multiple simulations either from the same initial configuration or from a completely independent initial configuration, as illustrated in Figure 12 for the N-400 melt under startup of shear flow at  $Wi = 80$ , although the positions of the fast and slow bands are randomly located. [Note that the DPD simulations are not deterministic as they contain a Brownian stochastic contribution to the equations of motion.] In actual experiments, flow is typically implemented by physical boundaries where one surface is moving and the opposing surface is stationary. In such a circumstance, it is physically reasonable that a fast band might always be induced to develop adjacent to the moving surface and a slow band adjacent to the stationary surface. In the DPD simulations, however, periodic boundary conditions are imposed such that there is no natural preference for band development at any specific location within the cell. Therefore, the fast and slow bands would tend to develop in localized regions of the simulation cell which were stochastically predisposed to such an event based on the vagaries of the initial configuration of the system and the random evolution of the stochastic process. Thus slow bands would tend to form where local chain disentanglement was less severe relative to other areas that ultimately experienced greater flow-induced disentanglement via whatever random events led to such an occurrence.

These points are evident in Fig. 12 for the N-400 melt under startup of shear flow at  $Wi = 80$ , which displays velocity profiles developed in three separate simulations. Here, R1 and R2 refer to completely independent initial system configurations, and S1 and S2 refer to two simulations using the same initial configuration (R2). Inset (II) demonstrates that even using the same quiescent initial configuration, the steady-state shear bands will evolve into mutually consistent fast and slow bands of equivalent relative widths, although the physical location of the bands will be randomly arranged along the  $y$ -dimension of the flow cell. This indicates that the width of the shear bands is not a stochastic effect, but is driven by a balance between the imposed flow kinematics and the free energy of the flowing system. Furthermore,

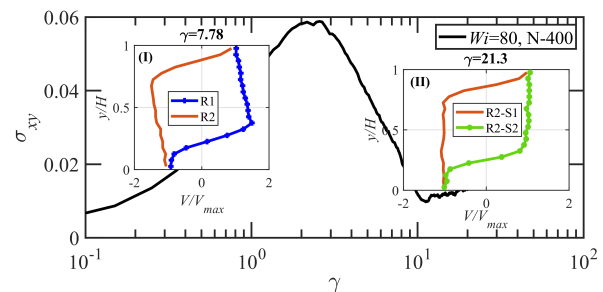


Fig. 12 Comparing the evolution of shear banding for the N-400 melt undergoing startup shear flow at  $Wi=80$  with different initial system configurations at equilibrium ( $t = 0$ ). The Inset (I) shows velocity profiles at  $\gamma = 7.8$  started from two different equilibrium configurations identified by R1 (red) and R2 (blue). Inset (II) shows the velocity profiles at  $\gamma = 21.7$  for two independent simulations (identified as R2-S1 (red) and R2-S2 (green)) started from the R2 equilibrium configuration. The difference in the locations of the fast band indicates the role of both stochastic and kinematic effects on the location of induced strain-rate zones over the  $y$ -direction.

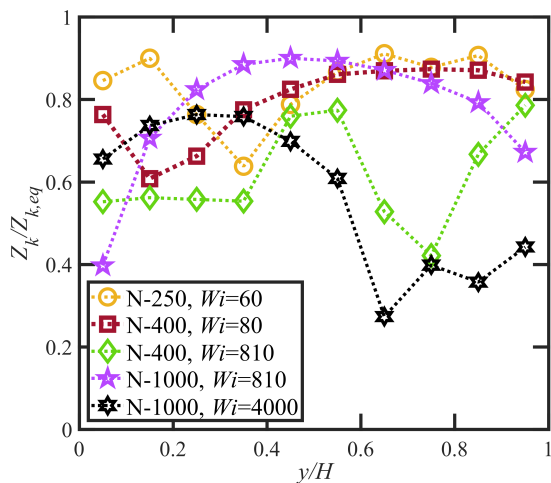


Fig. 13 Scaled mean kink number per chain averaged within respective sublayers of the simulation cell spanning the  $y$ -direction. At each  $Wi$ , the high values of  $Z_k/Z_{k,eq}$  correspond to sublayers within the steady-state slow band indicating greater kink density, and vice versa for sublayers within the fast band.

note that the RF effect observed in Inset (I) is not affected in any way by the stochastic nature of the flow evolution, either in terms of band location or strain (dimensionless time) units.

Figure 13 illustrates the scaled mean entanglement number per chain for macromolecules located within each of 10 sublayers in the gradient direction ( $y$ -direction) for all melts examined herein undergoing startup of shear flow at various  $Wi$ . The values of  $Z_k$  are scaled by the quiescent equilibrium kink entanglement number,  $Z_k^{eq}$ , for the respective chain length. The low points in all curves indicate the positions of the fast bands containing chains with lower entanglement density, whereas high values represent the position of the slow bands. Notably, compared with the slow bands where the number of entanglements is approximately similar to the equilibrium value, the fast bands obtain a lower average number of kinks per chain. Furthermore, an increase in molecular weight results in a larger difference between chain entanglement in the fast and slow bands. Note that the relative positions of the fast and slow bands within the simulation cell are essentially random from one simulation to the next, as discussed above.

Figure 14 presents the time evolution of the velocity profiles in the  $y$ -direction of the simulation cell at various values of strain units for all three PE melts undergoing startup of shear flow at a range of  $Wi$ . Also displayed in the figure are probability density functions of the scaled radius of gyration of the polymer chains,  $P(R_g/R_{max})$ , at various strain units of molecular chains occupying the slow and fast bands. For startup of shear flow of the N-250 melt at  $Wi = 60$  in Panel (a), the uniform velocity profile imposed at strain  $\gamma = 0$  begins to devolve into a two distinct bands of different strain rate immediately after the maximum is attained in the  $N_1$  time evolution at  $\gamma \approx 4$ . The velocity profile becomes very distinct by  $\gamma = 7.5$ , essentially attaining its steady-state shear-banded structure. Reverse flow is not observed in this N-250 melt. The PDFs of the scaled radius of gyration of molecules in the slow band shown in Panel (a-I) reveal that the slow band is comprised

of distributions of chains that remain close to their equilibrium PDFs throughout this process, whereas PDFs of chains in the fast band, Panel (a-II), reveal a dramatic extension of the constituent molecules from their quiescent PDF. The large breadth of these latter distributions is caused by the dynamic rotation/retraction of the quasiperiodic chain tumbling that occurs within the fast band.

The behavior of the N-400 and N-1000 melts at various  $Wi$  displayed in Fig. 14 are similar, and will be discussed collectively. Upon inception of shear flow, a uniform linear velocity profile is established throughout the simulation cell in the gradient direction with a shear rate consistent with the applied strain rate. At strain values shortly after the maximum in the time evolution of  $N_1$ , the velocity profile begins to devolve from the imposed linear profile. During the ensuing time period lasting about 3-5 strain units, reverse flow is observed as a section of the velocity profile of the slow band lying adjacent to the fast band exhibits a negative slope, indicating a negative velocity opposite to the direction of flow. This RF occurs during the window in which  $N_1$  is decreasing precipitously from its maximum value, indicating a strong recoil of the entangled chain network. As discussed above in reference to Fig. 7b, this window is marked by separation of  $N_1$  between the slow and fast bands. The PDFs of  $R_g/R_{max}$  in the slow bands reveal that the distributions of chain size remain close to their quiescent distributions throughout this process, but relax almost fully back to their quiescent distributions at the highest strain value displayed in various panels (I) of Fig. 14 (denoted with green dashed lines). Commensurately, the PDFs of molecules in the fast bands in panels (II) exhibit a quantitative similarity to those of the slow band at inception of shear band formation (blue dotted lines), but as time evolves these distributions shift to longer molecular extensions as the molecules stretch out and enter into quasiperiodic rotation and retraction cycles where the chain ends diffuse backward along the elongated molecules. Reverse flow occurs during this time period as the chains in the slow band recoil whereas those in the adjacent fast band elongate and eventually begin to rotate, as discussed in reference to Fig. 7(c),(d).

The individual chain  $\chi$  data plotted in Fig. 7(c),(d) were collected over the entire simulation cell by subdividing it into two parts, one corresponding to the (eventually developed) fast band and the other to the slow band. Focus can be directed at the interface by subdividing the cell into three slabs, one at the approximate interface and one on either side of it, corresponding to small regions in both the slow and fast bands, as shown in Figure 15. In this figure, individual chain dynamics are displayed for molecules with their centers of mass within three slabs of thickness  $y/H = 0.1$  centered at locations  $y/H = 0.5, 0.6, 0.7$ . These locations correspond to the narrow interfacial region, centered at  $y/H = 0.6$ , and the adjacent zones in the fast  $y/H = 0.7$  and slow bands  $y/H = 0.5$ . These panels thus allow for a very refined look at individual chain dynamics at and near the interface of the two distinct shear bands as they form after onset of flow and at the eventual steady-state. Note that the thick, black lines represent the mean relative extension of the chains within the respective subcells.

The observed behavior in Fig. 15 is very similar to that of

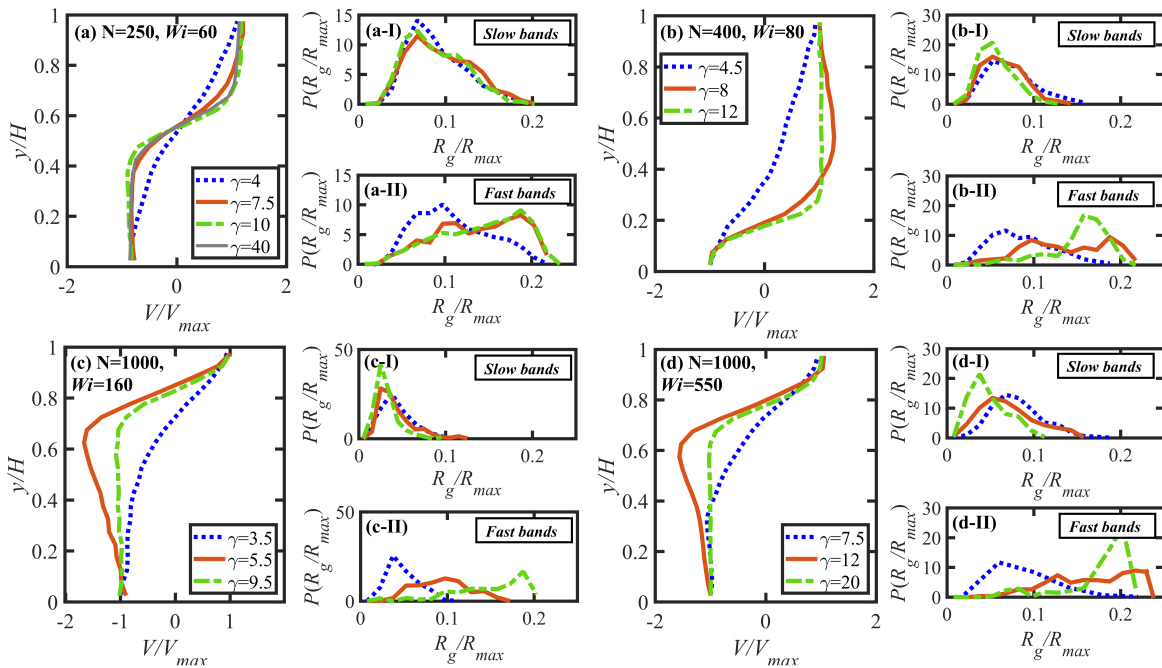


Fig. 14 Temporal evolution of the velocity profile with respect to the  $y$ -direction of the flow cell for the three PE melts under startup of shear flow at various  $Wi$  along with the probability distribution functions of the scaled radius of gyration,  $P(R_g/R_{max})$ , in the fast and slow bands at various strain values: (a)  $N=250$  melt at  $Wi=60$ , (b)  $N=400$  melt at  $Wi=80$ , (c)  $N=1000$  melt at  $Wi=160$ , and (d)  $N=1000$  melt at  $Wi=550$ .

Fig. 7(c),(d) on the whole, at least in the layers corresponding to the fast  $y/H = 0.7$  and slow bands  $y/H = 0.5$ . Chain dynamics here, even very close to the interface, very much resemble those of the larger subcells of fast and slow bands displayed in Fig. 7(c),(d); *i.e.*, chains in the fast band initially experience significant extension and then begin to tumble at longer times, whereas those in the slow band initially extend somewhat and then recoil to their individual steady-state value of  $\chi$ . Note, however, that in each zone, there are a small number of chains that display the dynamics of the opposite band. The situation in the interfacial zone centered at  $y/H = 0.6$ , however, is rather remarkable in that the individual chain dynamics display mostly a flow-aligning behavior, similar to those chains within the slow band, but with many of the chains displaying steady-state  $\chi$  values that are significantly higher than the chains within the slow band. In the interfacial region, only a few chains appear to be rotating, and this zone is evidently comprised primarily of chains that are more highly extended than those within the adjacent slow band, yet not experiencing any shear-induced chain tumbling cycles. Hence the observed behavior in the interfacial region is quite different than that observed in the adjacent narrow slow and fast bands, and one could describe it as a state of higher relative extension with arrested tumbling.

The same subdivision of the simulation cell can also be used to help understand the dynamical mechanisms underlying the reverse flow phenomenon by focusing in on the interface between the slow and fast bands, as illustrated in Figure 16. Panels (a),(b),(c) in this figure are the same data as Fig. 15 but with the small-strain portions of the graphs expanded for clarity. Also shown in this figure in Panels (d),(e),(f) is the time variation in

the number of chain kinks of the individual chains (thin colored lines) and the ensemble-averaged (thick black curve) number of kinks per chain,  $Z_k$ . The onset of reverse flow is denoted with the vertical dashed blue lines, and the extinction with dotted red lines. The onset of RF occurs at about the maximum in the  $N_1$  vs.  $\gamma$  curve, where the value of  $N_1$  in the slow band begins to diverge from that in the fast band—see Fig. 7(b). The behavior of  $\chi$  in the slow and fast bands is similar to that described above, with chains being stretched in the fast band but recoiling in the slow band. The most interesting aspect, however, is that within the interfacial region centered at  $y/H = 0.6$ , one observes a large number of chains undergoing both processes, rather than predominantly one or the other as in the adjacent subcells.

Plots of individual chain entanglement kink number vs. strain are displayed in Fig. 16(d),(e),(f). In the slow and fast bands, one observes the expected behavior, with a much smaller number of steady-state entanglements in the fast band as compared to the slow band. At the interface between the bands,  $Z_k$  is of intermediate value to these two extremes. Within the strain regime where reverse flow is exhibited, the behavior of  $Z_k$  is qualitatively similar within all subcells, indicating a direct correlation between chain extension and the number of entanglements it contains. Hence chains at the interface have insufficient number of entanglements to generate a reflexive recoil phenomenon, which induces a reverse flow within the slow band, but a sufficiently large number to arrest the tumbling motion of the chains such as occurs in the fast band. This explains the flow-aligning behavior of the interfacial chains and their wide distribution in relative extension. The recoiling experienced by chains in the slow band and commensurate stretching of chains in the fast band manifests at the inter-

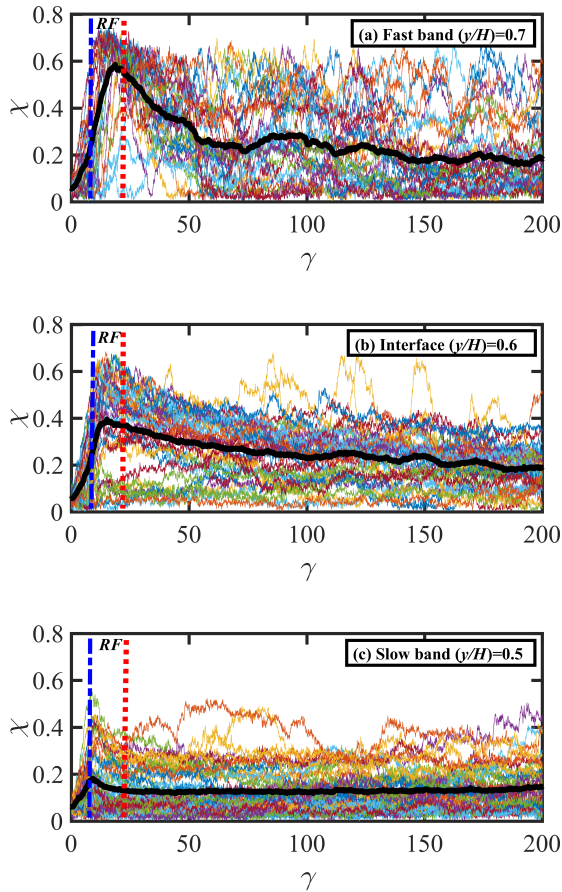


Fig. 15 Temporal evolution of ensemble-averaged relative extension  $\chi$  (black) and single-chain relative extension in three adjacent bands near the interface for the N-1000 melt at  $Wi = 550$ , where individual chains are denoted with random colors. The panels illustrate the dynamics of chains with their centers of mass located within layers of thickness  $y/H = 0.1$  at and near the interface between the slow and fast bands: (a) fast band at  $y/H = 0.7$ ; (b) interfacial band at  $y/H = 0.6$ ; and (c) slow band at  $y/H = 0.5$ . Note that the strain region where reverse flow is observed is identified by the dashed blue and dotted red vertical lines in each panel.

face as a very small stagnation region where the velocity passes through the null value, leading to a wide distribution of chain extension and orientation angle that are not varying greatly with time.

## 4 Conclusions

High-fidelity nonequilibrium dissipative particle dynamics simulations were used to investigate the transient and steady-state dynamic responses of highly entangled linear polyethylene melts subject to startup of shear flow over a broad range of strain rates. The coarse-grained DPD model<sup>54</sup> was used to generate entangled melts N-250, N-400, and N-1000 corresponding to monodisperse linear PE liquids  $C_{750}H_{1502}$ ,  $C_{1200}H_{2402}$ , and  $C_{3000}H_{6002}$ , respectively. Principal conclusions of this study are summarized in the bulleted list below.

- The steady-state shear stress profile displayed a nonmonotonic behavior with a local maximum at  $\dot{\gamma} \approx 10\tau_d^{-1}$  and a local minimum at  $\dot{\gamma} \sim \tau_R^{-1}$ ; *i.e.*, on the order of  $\tau_R^{-1}$  but not necessarily equivalent to  $\tau_R^{-1}$ .
- Shear banding was not observed under startup of shear flow for the PE melts when  $\dot{\gamma} < 10\tau_d^{-1}$  or when  $\dot{\gamma} > \tau_e^{-1}$ . At  $\dot{\gamma} < 10\tau_d^{-1}$ , the flow was too weak to generate the entanglement destruction and molecular extension required for individual chain mobility leading to the induced rotation/retraction cycles of molecules comprising the fast band. At  $\dot{\gamma} > \tau_e^{-1}$ , the flow was strong enough to quickly destroy the entanglement network before the slow band could develop. In these cases, a uniform linear velocity profile was generated shortly after inception of flow with a slope that was consistent with the imposed shear rate, which persisted throughout startup until steady state was attained.
- The shear stress profile computed from various sublayers of the simulation cell spanning the  $y$ -direction was constant in all cases, regardless of whether or not shear banding occurred.
- Steady-state shear banding was observed for all melts within the range  $10\tau_d^{-1} < \dot{\gamma} < \tau_e^{-1}$ , although only transient shear banding was observed as  $\dot{\gamma} \rightarrow \tau_e^{-1}$ . In this latter shear rate region, the rate of entanglement destruction in the temporary fast band occurred faster than in the temporary slow band, leading to shear bands that ultimately dissipated as the entire system approached steady state. Steady-state observations of the entanglement number revealed a much lower degree of entanglement in the fast band relative to the slow band.
- The onset of shear banding was associated with a local maximum in the time evolution of the first normal stress difference, which followed a similar overshoot in the shear stress by several strain units. The maximum in  $N_1$  corresponded with the beginning of molecular recoil in the slow band.
- Steady-state shear bands formed at various flow state points on the line of constant shear stress that was generated throughout the cell in the  $y$ -direction at each  $Wi$ . Within the region of nonmonotonicity of the shear stress, three possible flow state points of constant shear stress were available to the flowing melt system. Under startup of shear at different applied shear rates, the system would develop slow and fast

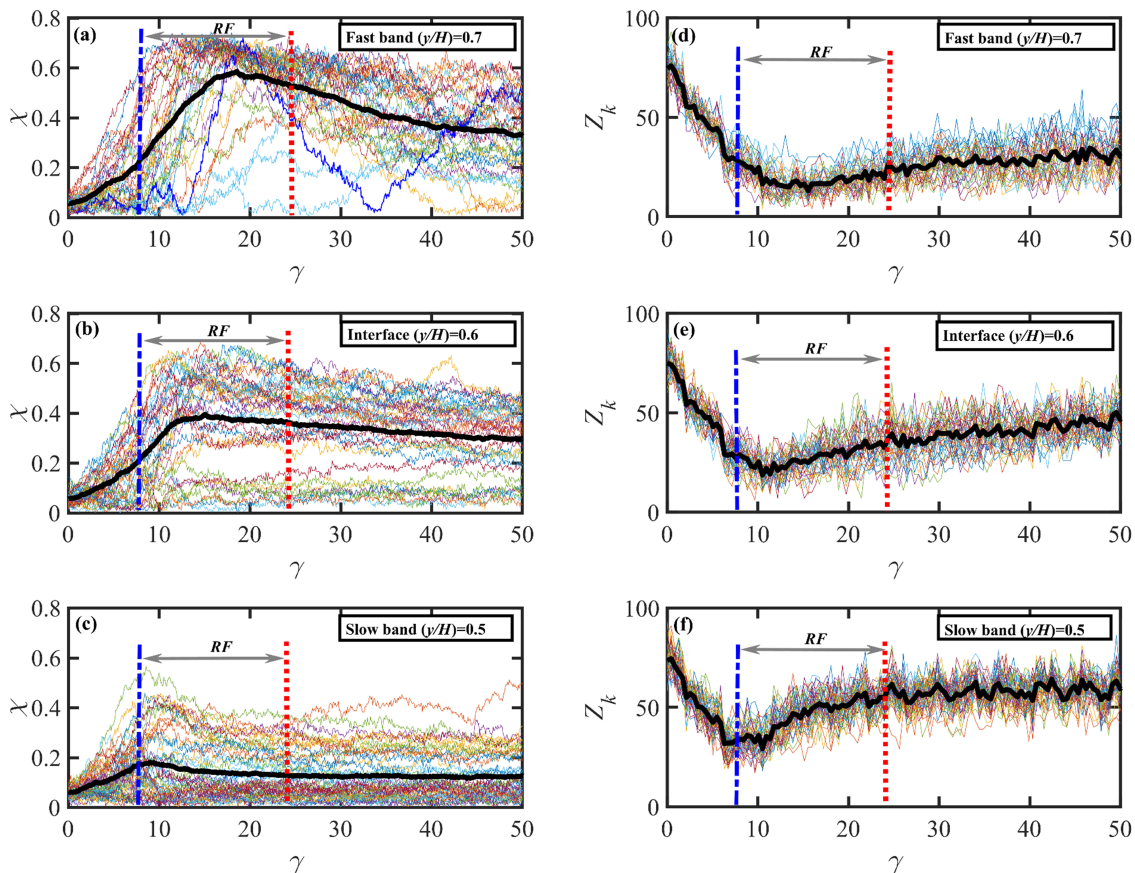


Fig. 16 Temporal evolution of ensemble-averaged relative extension  $\chi$  (black) and single-chain relative extension in three adjacent bands near the interface for the N-1000 melt at  $Wi = 550$ , where individual chains are denoted with random colors. The panels illustrate the dynamics of chains with their centers of mass located within layers of thickness  $y/H = 0.1$  at and near the interface between the slow and fast bands: (a) fast band at  $y/H = 0.7$ ; (b) interfacial band at  $y/H = 0.6$ ; and (c) slow band at  $y/H = 0.5$ . Panels (d), (e), and (f) display temporal data for individual chain entanglement kink number (thin colored lines),  $Z_k$ , and the ensemble average (thick black lines) within the same three subcells as described above. Note that the strain region where reverse flow is observed is identified by the dashed blue and dotted red vertical lines in each panel.

bands that were compatible with two of these available state points of constant shear stress, possibly at random. However, a general trend seemed to be that below the minimum in the shear stress curve, the slow band corresponded to the left state point in Fig. 8, whereas it usually corresponded to the middle point for applied  $Wi$  greater than the minimum. The fast band always assumed the right state point, although this cannot be stated definitively because of the limited nature of the simulated  $Wi$  range.

- The fast and slow bands were formed in localized regions where the stochastic nature of the dynamics resulted in domains of relatively fewer or more entanglements that impacted the localized individual chain dynamics. Molecules in the fast band experienced fewer entanglements and more mobility and extension, whereas those in the slow band tended to recoil toward less extended and more coiled configurations. In spite of this, bands formed under identical startup conditions but in separate simulations were observed at random positions in the  $y$ -direction, but maintained a

common width, indicating a balance between flow kinematics and the inherent free energy of the PE melt.

- In most simulations of the N-400 and N-1000 melts, a reverse flow (corresponding to a negative local velocity) was observed during the period of recoil of molecules in the slow band. This behavior was not observed in the N-250 melt, presumably because the chains were insufficiently long to generate a substantial degree of recoil.
- The width of the fast band generally increased with increasing  $Wi$ , ranging in size from about 20% of the flow cell width in the  $y$ -direction to 40-50% at high  $Wi$ . This increase in size was associated with a greater number of highly mobile (*i.e.*, relatively disentangled) chains at higher flow strength. The width of the fast band was larger as chain length increased (likely due to an increase in the inherent  $R_{g,yy}$  component of the gyration tensor), but still followed this general trend in relative size with respect to the flow cell. However, the limited data also demonstrated that the width of the fast

band was about 20% of the  $y$ -dimension of the simulation cell when the slow band is at the left state point and is 40–50% of the  $y$ -dimension when the slow band is at the middle state point, pointing to a possible free energy effect.

As a last point of consideration, it has been demonstrated previously that polydisperse systems display less significant nonmonotonic steady-state shear stress profiles than the monodisperse samples simulated in this work<sup>41</sup>. This is because the range of times scales associated with chain stretching and rotation of molecules of differing length, which smears out the nonmonotonic nature of the shear stress curve over the intermediate shear rate regime, leading to a shear stress plateau of very low slope, similar to that of the  $N_1$  profile evident in Fig. 2(c). Hence for polydisperse systems, the flow state points evident in Fig. 8 are not clearly defined, and therefore also presumably less stable. Hence polydisperse systems are more likely to exhibit only transient shear banding as the system passes through the (low-slope) plateau strain-rate range and then eventually settle into a unique state point at the assigned stress value. In cases where the slope of the shear stress curve is vanishingly small, a multiplicity of states would be available to the system, which might be close enough energetically to be susceptible to temporary fluctuations that would give rise to a system in which no stable steady-state could be achieved, but in which the system fluctuated over time from one shear-banded state to another. Furthermore, by imposing startup of shear under conditions of time-ramped strain rates, it is possible to observe a hysteresis effect upon ramping the shear rate back down since the flow bands assumed on the upward ramp might not be the same as developed on the downward ramp. Clearly, further investigation remains necessary to understand fully the shear-banding phenomenon in polymer melts.

### Conflicts of interest

The authors declare that there are no conflicts of interest.

### Acknowledgements

Financial support was provided by the National Science Foundation under grant CBET-1602890. The simulations were partially performed on the computational resources at the Infrastructure for Scientific Applications and Advanced Computing (ISAAC), supported by the University of Tennessee-Knoxville, and SUMMIT at the ORNL Leadership Computing Facility (OLCF). This work also used resources of Anvil and the Frontera computing project at the Texas Advanced Computing and Extreme Science and Engineering Discovery Environment (XSEDE), which are supported by NSF under grants ACI-1548562 and TG-CTS150054.

### Notes and references

- 1 S. M. Fielding, *Soft Matter*, 2007, **3**, 1262–1279.
- 2 T. Divoux, M. A. Fardin, S. Manneville and S. Lerouge, *Ann. Rev. Fluid Mech.*, 2016, **48**, 81–103.
- 3 P. D. Olmsted, *Rheol. Acta*, 2008, **47**, 283–300.
- 4 S. Lerouge and P. D. Olmsted, *Front. Phys.*, 2020, 246.
- 5 P. Tapadia, S. Ravindranath and S.-Q. Wang, *Phys. Rev. Lett.*, 2006, **96**, 196001.
- 6 P. E. Boukany and S.-Q. Wang, *Macromolecules*, 2008, **41**, 1455–1464.
- 7 M. C. Burroughs, Y. Zhang, A. M. Shetty, C. M. Bates, L. G. Leal and M. E. Helgeson, *Phys. Rev. Lett.*, 2021, **126**, 207801.
- 8 S. Shin, K. D. Dorfman and X. Cheng, *Physical Review E*, 2017, **96**, 062503.
- 9 M. E. Cates and S. M. Fielding, *Adv. Phys.*, 2006, **55**, 799–879.
- 10 J.-F. Berret, *Molecular Gels*, Springer, 2006, pp. 667–720.
- 11 M. E. Helgeson, M. D. Reichert, Y. T. Hu and N. J. Wagner, *Soft Matter*, 2009, **5**, 3858–3869.
- 12 J. M. Adams and D. Corbett, *Phys. Rev. E*, 2018, **97**, 052601.
- 13 B. Zielinska and A. Ten Bosch, *Phys. Rev. A*, 1988, **38**, 5465.
- 14 C. Denniston, E. Orlandini and J. Yeomans, *Phys. Rev. E*, 2001, **63**, 056702.
- 15 H. Rehage and H. Hoffmann, *Mol. Phys.*, 1991, **74**, 933–973.
- 16 S. Fielding, M. Cates and P. Sollich, *Soft Matter*, 2009, **5**, 2378–2382.
- 17 M. Cromer, M. C. Villet, G. H. Fredrickson and L. G. Leal, *Phys. Fluids*, 2013, **25**, 051703.
- 18 S. Caserta, M. Simeone and S. Guido, *Phys. Rev. Lett.*, 2008, **100**, 137801.
- 19 P.-G. de Gennes, *J. Chem. Phys.*, 1971, **55**, 572–579.
- 20 M. Doi and S. Edwards, *J. Chem. Soc., Faraday Trans. 2: Mol. Chem. Phys.*, 1978, **74**, 1802–1817.
- 21 N. Spenley, X. Yuan and M. Cates, *J. Phys. II*, 1996, **6**, 551–571.
- 22 J. K. Dhont, *Phys. Rev. E*, 1999, **60**, 4534.
- 23 A. E. Likhtman and R. S. Graham, *J. Non-Newtonian Fluid Mech.*, 2003, **114**, 1–12.
- 24 J. Adams, S. M. Fielding and P. D. Olmsted, *J. Rheol.*, 2011, **55**, 1007–1032.
- 25 S. Fielding and P. Olmsted, *Phys. Rev. Lett.*, 2006, **96**, 104502.
- 26 R. L. Moorcroft and S. M. Fielding, *Phys. Rev. Lett.*, 2013, **110**, 086001.
- 27 R. L. Moorcroft and S. M. Fielding, *J. Rheol.*, 2014, **58**, 103–147.
- 28 R. L. Moorcroft, M. E. Cates and S. M. Fielding, *Phys. Rev. Lett.*, 2011, **106**, 055502.
- 29 J. Adams and P. D. Olmsted, *Phys. Rev. Lett.*, 2009, **102**, 067801.
- 30 P. E. Boukany and S.-Q. Wang, *J. Rheol.*, 2009, **53**, 73–83.
- 31 P. E. Boukany, S.-Q. Wang and X. Wang, *Macromolecules*, 2009, **42**, 6261–6269.
- 32 S.-Q. Wang, S. Ravindranath and P. Boukany, *Macromolecules*, 2011, **44**, 183–190.
- 33 P. E. Boukany, S.-Q. Wang, S. Ravindranath and L. J. Lee, *Soft Matter*, 2015, **11**, 8058–8068.
- 34 P. E. Boukany and S.-Q. Wang, *Soft Matter*, 2009, **5**, 780–789.
- 35 S. Manneville, *Rheol. Acta*, 2008, **47**, 301–318.
- 36 J. Cao and A. E. Likhtman, *Phys. Rev. Lett.*, 2012, **108**, 028302.
- 37 M. Mohagheghi and B. Khomami, *J. Rheol.*, 2016, **60**, 849–859.

- 38 M. Mohagheghi and B. Khomami, *J. Rheol.*, 2016, **60**, 861–872.
- 39 M. Mohagheghi and B. Khomami, *Phys. Rev. E*, 2016, **93**, 062606.
- 40 M. Mohagheghi and B. Khomami, *ACS Macro Lett.*, 2015, **4**, 684–688.
- 41 M. Boudaghi-Khajehnohar, B. J. Edwards and B. Khomami, *Soft Matter*, 2020, **16**, 6468–6483.
- 42 C. M. Schroeder, H. P. Babcock, E. S. Shaqfeh and S. Chu, *Science*, 2003, **301**, 1515–1519.
- 43 T. T. Perkins, D. E. Smith and S. Chu, *Science*, 1997, **276**, 2016–2021.
- 44 D. E. Smith and S. Chu, *Science*, 1998, **281**, 1335–1340.
- 45 S. Shin, Y. Kou, K. D. Dorfman and X. Cheng, *Macromolecules*, 2021, **54**, 4186–4197.
- 46 M. H. Nafar Sefiddashti, B. J. Edwards and B. Khomami, *Polymers*, 2019, **11**, 476.
- 47 M. H. Nafar Sefiddashti, B. J. Edwards and B. Khomami, *Phys. Rev. Fluids*, 2017, **2**, 083301.
- 48 M. H. Nafar Sefiddashti, B. J. Edwards and B. Khomami, *J. Rheol.*, 2015, **59**, 119–153.
- 49 M. H. Nafar Sefiddashti, B. J. Edwards and B. Khomami, *J. Rheol.*, 2016, **60**, 1227–1244.
- 50 M. H. Nafar Sefiddashti, B. J. Edwards and B. Khomami, *Macromolecules*, 2020, **53**, 6432–6451.
- 51 C. N. Edwards, M. H. Nafar Sefiddashti, B. J. Edwards and B. Khomami, *J. Mol. Graph. Model.*, 2018, **81**, 184–196.
- 52 J. M. Kim, B. J. Edwards, D. J. Keffer and B. Khomami, *J. Rheol.*, 2010, **54**, 283–310.
- 53 B. J. Edwards, M. H. Nafar Sefiddashti and B. Khomami, *J. Rheol.*, 2022, **66**, 415–489.
- 54 M. H. N. Nafar Sefiddashti, M. Boudaghi-Khajehnohar, B. J. Edwards and B. Khomami, *Sci. Rep.*, 2020, **10**, 1–13.
- 55 P. J. Hoogerbrugge and J. M. V. A. Koelman, *Europhys. Lett.*, 1992, **19**, 155–160.
- 56 J. M. V. A. Koelman and P. J. Hoogerbrugge, *Europhys. Lett.*, 1993, **21**, 363–368.
- 57 P. Español and P. Warren, *Europhys. Lett.*, 1995, **30**, 191.
- 58 R. D. Groot and P. B. Warren, *J. Chem. Phys.*, 1997, **107**, 4423–4435.
- 59 M. Boudaghi, M. H. Nafar Sefiddashti, B. J. Edwards and B. Khomami, *J. Rheol.*, 2022, **66**, 551–569.
- 60 S. Plimpton, *J. Comp. Phys.*, 1995, **117**, 1–19.
- 61 G. T. Dee, T. Ougizawa and D. J. Walsh, *Polymer*, 1992, **33**, 3462–3469.
- 62 P. Nikunen, I. Vattulainen and M. Karttunen, *Phys. Rev. E*, 2007, **75**, 036713.
- 63 J. Irving and J. G. Kirkwood, *J. Chem. Phys.*, 1950, **18**, 817–829.
- 64 M. Doi and S. F. Edwards, *The Theory of Polymer Dynamics*, Oxford University Press, New York, 1986.
- 65 M. Kröger, *Comp. Phys. Comm.*, 2005, **168**, 209–232.
- 66 S. Shanbhag and M. Kröger, *Macromolecules*, 2007, **40**, 2897–2903.
- 67 N. C. Karayiannis and M. Kröger, *Int. J. Mol. Sci.*, 2009, **10**, 5054–5089.
- 68 M. Kröger, J. D. Dietz, R. S. Hoy and C. Luap, *Computer Physics Communications*, 2023, **283**, 108567.
- 69 J. T. Padding and W. J. Briels, *J. Chem. Phys.*, 2001, **115**, 2846–2859.
- 70 R. Everaers, *Phys. Rev. E*, 2012, **86**, 022801.
- 71 J. Kim, B. Edwards, D. J. Keffer and B. Khomami, *Phys. Lett. A*, 2009, **373**, 769–772.
- 72 J. Kim, P. S. Stephanou, B. Edwards and B. Khomami, *J. Non-Newtonian Fluid Mech.*, 2011, **166**, 593–606.
- 73 B. J. Edwards, M. H. Nafar Sefiddashti and B. Khomami, *J. Rheol.*, 2022, **66**, 415–489.
- 74 M. H. Nafar Sefiddashti, B. J. Edwards and B. Khomami, *Phys. Rev. Res.*, 2020, **2**, 013035.
- 75 M. H. Nafar Sefiddashti, B. J. Edwards and B. Khomami, *Phys. Rev. Lett.*, 2018, **121**, 247802.
- 76 M. H. Nafar Sefiddashti, B. J. Edwards and B. Khomami, *J. Chem. Phys.*, 2018, **148**, 141103.
- 77 M. H. Nafar Sefiddashti, B. J. Edwards and B. Khomami, *Phys. Rev. Res.*, 2020, **2**, 013035.
- 78 M. H. Nafar Sefiddashti, B. J. Edwards and B. Khomami, *Macromolecules*, 2020, **53**, 10487–10502.
- 79 K. Sato, X.-F. Xuan and T. Kawakatsu, *Eur. Phys. J. E*, 2010, **31**, 135–144.
- 80 S. M. Fielding, *Soft Matter*, 2007, **3**, 1262–1279.